

An rp -adaptive method for accurate resolution of shock-dominated viscous flow based on implicit shock tracking

Huijing Dong^{a,1}, Masayuki Yano^{b,2}, Tianci Huang^{a,3}, Matthew J. Zahr^{a,4,*}

^aDepartment of Aerospace and Mechanical Engineering, University of Notre Dame, Notre Dame, IN 46556, United States

^bInstitute for Aerospace Studies, University of Toronto, Toronto, M3H 5T6, Ontario, Canada

Abstract

This work introduces an optimization-based rp -adaptive numerical method to approximate solutions of viscous, shock-dominated flows using implicit shock tracking and a high-order discontinuous Galerkin discretization on traditionally coarse grids without nonlinear stabilization (e.g., artificial viscosity or limiting). The proposed method adapts implicit shock tracking methods, originally developed to align mesh faces with solution discontinuities, to compress elements into viscous shocks and boundary layers, functioning as a novel approach to aggressive r -adaptation. This form of r -adaptation is achieved naturally as the minimizer of the enriched residual with respect to the discrete flow variables and coordinates of the nodes of the grid. Several innovations to the shock tracking optimization solver are proposed to ensure sufficient mesh compression at viscous features to render stabilization unnecessary, including residual weighting, step constraints and modifications, and viscosity-based continuation. Finally, p -adaptivity is used to locally increase the polynomial degree with three clear benefits: (1) lessens the mesh compression requirements near shock waves and boundary layers, (2) reduces the error in regions where r -adaptivity is not sufficient with the given grid topology, and (3) reduces computational cost by performing a majority of the r -adaptivity iterations on the coarsest discretization. A series of numerical experiments show the proposed method effectively resolves viscous, shock-dominated flows, including accurate prediction of heat flux profiles produced by hypersonic flow over a cylinder, and compares favorably in terms of accuracy per degree of freedom to h -adaptation with a high-order discretization.

Keywords: Shock fitting, discontinuous Galerkin, r -adaptivity, p -adaptivity, shock-dominated flows, hypersonic flows

1. Introduction

Computational fluid dynamics (CFD) has become an essential tool for gaining a deeper understanding of flow physics and enabling the prediction and control of complex fluid flows. However, high-speed flows, particularly in the hypersonic regime, present significant challenges even for modern CFD methods. One major difficulty is their sensitivity to the computational mesh as tight grid spacing near and precise alignment with shock waves and boundary layers are needed [32, 9, 20, 8]. Properly aligning the grid with shocks is a user-intensive process, often requiring iterating between grid generation and flow simulation [9]. Additionally, nonlinear instabilities become increasingly problematic as the Mach number and vehicle bluntness increase [10], which further complicates the stability and accuracy of numerical methods.

Shock-dominated flows are typically handled using shock capturing methods, which employ various techniques to stabilize the numerical solution on a fixed computational grid while preserving shock structures.

*Corresponding author

Email addresses: hdong2@nd.edu (Huijing Dong), masa.yano@utoronto.ca (Masayuki Yano), thuang5@alumni.nd.edu (Tianci Huang), mzahr@nd.edu (Matthew J. Zahr)

¹Graduate Student, Department of Aerospace and Mechanical Engineering, University of Notre Dame

²Associate Professor, Institute for Aerospace Studies, University of Toronto

³Research Associate, Department of Aerospace and Mechanical Engineering, University of Notre Dame

⁴Assistant Professor, Department of Aerospace and Mechanical Engineering, University of Notre Dame

One common approach involves the use of limiters, which are widely applied in second-order finite volume methods to prevent spurious oscillations [47]. Another widely used method is Weighted Essentially Non-Oscillatory (WENO) [21, 27, 33] schemes, which reconstruct high-resolution solutions using different stencils to mitigate numerical oscillations. However, WENO is most effective on Cartesian grids, thus making it less suitable for flows around complex geometries. Artificial viscosity is perhaps the most popular approach in the high-order community. These approaches selectively add artificial viscosity to elements where oscillatory behavior is detected using a shock sensor [43, 17, 4, 12]. For high Mach flows, greater levels of artificial viscosity are required, which introduces the challenge of balancing stabilization with solution accuracy. Excessive artificial viscosity can alter shock structure, affecting boundary layer characteristics and potentially leading to inaccurate predictions of aerodynamic heating in the hypersonic regime [10, 32].

On the other hand, shock-fitting methods align the computational mesh with solution discontinuities to represent them perfectly without additional stabilization. Such techniques can generate highly accurate solutions on coarse meshes, especially when combined with high-order numerical methods. Traditional shock-fitting methods, use the Rankine–Hugoniot conditions to compute the shock speed and the downstream state, and subsequently determine the shock motion [37, 45, 13, 7, 19]. A major challenge of this approach is the need to generate a fitted mesh that conforms to the shock surface, which becomes increasingly difficult as the complexity of the shock topologies increase, making it unsuitable for some complex flows [28]. Efforts to extend shock-fitting methods to viscous flows, where shock waves are rapid transitions⁵ over a finite thickness, approximate shocks as discontinuities, thereby neglecting their thickness and internal structure [3, 38]. Moretti [38] argues that this is the only viable approach to handle high Reynolds flows; however, the internal shock structure is governed by complex thermochemical effects and neglecting them could lead to inaccurate predictions of shock-boundary-layer interactions, aerodynamic heating, and post-shock thermodynamic states, particularly for low Reynolds number flows.

A new class of high-order methods, implicit shock tracking, that includes moving discontinuous Galerkin method with interface condition enforcement (MDG-ICE) [14, 31, 30, 11] and high-order implicit shock tracking (HOIST) method [51, 53, 26, 46, 39, 25] have overcome the key limitation of traditional shock-fitting methods by discretizing the conservation law on a shock-agnostic mesh and simultaneously computing the discrete flow field and coordinates of the mesh nodes as the solution of an optimization problem. This key innovation has led to general approaches that is equation- and problem-independent, capable of aligning grids with complex shock structures, and recovering the design-order of the numerical discretization for non-smooth flows. The MDG-ICE method, originally developed for inviscid flows where shocks are discontinuities, has been extended to an aggressive r -adaptive method capable of resolving the internal structure of viscous shocks and boundary layers by compressing elements into the transition [31, 30, 11]. By using a sufficiently large polynomial degree for both the solution and mesh, these features are accurately resolved with a single, highly stretched element. The viscous variant of the MDG-ICE method uses a novel variational formulation that write conservation, the jump condition, and the viscous constitutive law in their strong, first-order (flux) form. They introduce independent test variables for each equation, which leads to four residuals that are simultaneously minimized. This approach is elegant, directly connected to the equations governing shock-dominated viscous flow, and has been shown to accurately resolve challenging viscous flows in two- and three-dimensions. However, it suffers from two drawbacks. First, the flux formulation requires simultaneous computation of the flow variables and their gradient, which increases the number of discrete unknowns by a factor of $d + 1$ in d dimensions, which can make the linearized system prohibitively large. Second, the viscous MDG-ICE method requires high-degree (usually $p \geq 4$) polynomials to accurately approximate the internal structure of shocks and boundary layers with a single element, but high-degree polynomials are unnecessary in the regions away from these viscous transitions where flow field is constant or slowly varying.

In this work, we introduce an rp -adaptive discretization as an extension of the HOIST method that addresses the aforementioned limitations of the viscous MDG-ICE method. First, our method uses the primal form of a standard interior penalty discontinuous Galerkin (IPDG) [1, 2, 23, 24] to eliminate auxiliary variables prior to discretization, which amounts to a savings factor of $d + 1$ in terms of degrees of freedom.

⁵Throughout this work, we define a *transition* as a continuous flow feature bridging distinct states. The strength of a transition is proportional to the magnitude difference between the two states and inversely proportional to the distance over which the transition occurs.

The implicit shock tracking problem is formulated as an optimization problem over the discrete flow variables and mesh nodal coordinates. The optimization problem minimizes the IPDG residual with an enriched test space and it is constrained by the IPDG equations to ensure the properties of IPDG (stability, high-order accuracy, consistency, adjoint consistency) [2, 23] are inherited. To ensure both the shock wave and boundary layer are given similar priority by the minimum-residual method, despite the shock wave being a stronger feature (in terms of the magnitude of the transition and transition width), the residual contribution of all elements touching a viscous wall are amplified. The optimization problem is embedded in a viscosity continuation loop, similar to that in [31], which proved critical for robust element compression into viscous transitions and to avoid carbuncles. On its own, the proposed framework functions as an aggressive r -adaptive method in primal form to accurately resolve viscous shock-dominated flows, where nodes are adjusted during the nonlinear solve (as opposed to the more common approach of moving nodes *a posteriori* after the solve is complete). To avoid the need for excessive mesh compression or a large constant polynomial degree across the domain, the entire framework is further embedded in a p -adaptivity setting to iteratively increase the polynomial degree in underresolved regions. Experimentation with several error indicators revealed the enriched residual, which defines the shock tracking objective function, is the most effective because it rapidly increased the polynomial degree inside the viscous features so they can be resolved with one or two elements, then focused the p -refinement to other underresolved features. Finally, the underlying optimization problem is solved using the sequential quadratic programming method proposed in [54, 26] with several robustness enhancements required to compress elements to a small fraction of their original size. These robustness measures include step length constraints, step modifications, and a new regularization strategy for the Levenberg–Marquardt Hessian approximation.

The remainder of this paper is organized as follows. Section 2 introduces the governing system of compressible viscous conservation law, its reformulation on a fixed reference domain, and its discretization using an IPDG method; the section also reviews solution-based error estimation and p -adaptivity. Section 3 extends the implicit shock tracking formulation originally proposed in [51, 54, 26] to incorporate continuation and p -adaptivity. It also introduces several robustness enhancements to the optimization solver in [26] necessary to robustly compress mesh elements into thin shock waves and boundary layers. Section 4 presents a series of numerical experiments that demonstrate the capability of the proposed rp -adaptive to accurately resolve shock-dominated viscous flows, including hypersonic flow over a cylinder with accurate heat flux profile predictions. It also systematically studies several of the solver innovations proposed in this work to directly demonstrate their impact. Section 5 offers conclusions.

2. Governing equations and high-order discretization

In this section, we introduce the governing equations (steady or space-time, viscous conservation law) (Section 2.1) and recast them over a fixed reference domain such that domain deformations appear explicitly (Section 2.2). The transformed conservation law is discretized using a high-order IPDG method (Section 2.3). We close the section with a review of standard *a posteriori* error indicators (Section 2.4).

2.1. System of viscous conservation laws

A general system of m steady viscous conservation laws, defined in spatial domain $\Omega \subset \mathbb{R}^d$ takes the form

$$\nabla \cdot F(U, \nabla U) = S(U, \nabla U) \quad \text{in } \Omega, \quad (1)$$

where $U : \Omega \rightarrow \mathbb{R}^m$, $U : x \mapsto U(x)$ is the solution of the system of conservation laws, $F : \mathbb{R}^m \times \mathbb{R}^{m \times d} \rightarrow \mathbb{R}^{m \times d}$ is the flux function, and $S : \mathbb{R}^m \times \mathbb{R}^{m \times d} \rightarrow \mathbb{R}^m$ is the source term, and $\nabla := (\partial_{x_1}, \dots, \partial_{x_d})$ is the gradient operator in the physical domain. The formulation of the conservation law in (1) is sufficiently general to encapsulate steady conservation laws in a d -dimensional spatial domain or time-dependent conservation laws in a $(d - 1)$ -dimensional domain, i.e., a d -dimensional space-time domain.

We assume the flux function can be split into an inviscid and viscous term as

$$F(W, Q) = F_{\text{inv}}(W) - F_{\text{visc}}(W, Q), \quad (2)$$

for any $W \in \mathbb{R}^m$ and $Q \in \mathbb{R}^{m \times d}$, where $F_{\text{inv}} : \mathbb{R}^m \rightarrow \mathbb{R}^{m \times d}$, $F_{\text{inv}} : W \mapsto F_{\text{inv}}(W)$ is the inviscid flux function and $F_{\text{visc}} : \mathbb{R}^m \times \mathbb{R}^{m \times d} \rightarrow \mathbb{R}^{m \times d}$, $F_{\text{visc}} : (W, Q) \mapsto F_{\text{visc}}(W, Q)$ is the viscous flux function, which reduces (1)

to

$$\nabla \cdot F_{\text{inv}}(U) - \nabla \cdot F_{\text{visc}}(U, \nabla U) = S(U, \nabla U). \quad (3)$$

Additionally, we assume the viscous term is linear in its second argument

$$F_{\text{visc}}(W, Q) = D(W) : Q, \quad (4)$$

for any $W \in \mathbb{R}^m$ and $Q \in \mathbb{R}^{m \times d}$, where $D : \mathbb{R}^m \rightarrow \mathbb{R}^{m \times d \times m \times d}$ is the viscous tensor.

2.2. Transformed conservation laws on a fixed reference domain

Before introducing a discretization of (3), it is convenient to transform domain of the conservation law Ω to a fixed reference domain $\Omega_0 \subset \mathbb{R}^d$. Let \mathbb{G} be the collection of diffeomorphisms from the reference domain to the physical domain; i.e., for any $\mathcal{G} \in \mathbb{G}$, $\mathcal{G} : \Omega_0 \rightarrow \Omega$. Then the conservation law on the physical domain is transformed to a conservation law on the reference domain as

$$\bar{\nabla} \cdot \bar{F}_{\text{inv}}(\bar{U}; G) - \bar{\nabla} \cdot \bar{F}_{\text{visc}}(\bar{U}, \bar{\nabla} \bar{U}; G) = \bar{S}(\bar{U}, \bar{\nabla} \bar{U}; G) \quad \text{in } \Omega_0, \quad (5)$$

where $\bar{U} : \Omega_0 \rightarrow \mathbb{R}^m$, $\bar{U} : X \mapsto \bar{U}(X)$ is the solution of the transformed conservation law, $\bar{F}_{\text{inv}} : \mathbb{R}^m \times \mathbb{R}^{d \times d} \rightarrow \mathbb{R}^{m \times d}$ is the transformed inviscid flux function, $\bar{F}_{\text{visc}} : \mathbb{R}^m \times \mathbb{R}^{m \times d} \times \mathbb{R}^{d \times d} \rightarrow \mathbb{R}^{m \times d}$ is the transformed viscous flux function, $\bar{S} : \mathbb{R}^m \times \mathbb{R}^{m \times d} \times \mathbb{R}^{d \times d} \rightarrow \mathbb{R}^m$ is the transformed source term, and $\bar{\nabla} := (\partial_{X_1}, \dots, \partial_{X_d})$ is the gradient operator in the reference domain. The deformation gradient $G : \Omega_0 \rightarrow \mathbb{R}^{d \times d}$ is defined as

$$G : X \mapsto \bar{\nabla} \mathcal{G}(X). \quad (6)$$

The reference domain solution is related to the solution over the physical domain as

$$\bar{U}(X) = U(\mathcal{G}(X)), \quad \bar{\nabla} \bar{U}(X) = \nabla U(\mathcal{G}(X))G(X). \quad (7)$$

for any $X \in \Omega_0$. The fluxes and source terms transform as

$$\begin{aligned} \bar{F}_{\text{inv}} : (\bar{W}; \Theta) &\mapsto \det(\Theta) F_{\text{inv}}(\bar{W}) \Theta^{-T} \\ \bar{F}_{\text{visc}} : (\bar{W}, \bar{Q}; \Theta) &= \det(\Theta) F_{\text{visc}}(\bar{W}, \bar{Q} \Theta^{-1}) \Theta^{-T} \\ \bar{S} : (\bar{W}, \bar{Q}; \Theta) &= \det(\Theta) S(\bar{W}, \bar{Q} \Theta^{-1}). \end{aligned} \quad (8)$$

The transformed viscous flux maintains linearity with respect to the state gradient; i.e.,

$$\bar{F}_{\text{visc}}(\bar{W}, \bar{Q}; \Theta) = \bar{D}(\bar{W}; \Theta) : \bar{Q}, \quad (9)$$

for any $\bar{W} \in \mathbb{R}^m$, $\bar{Q} \in \mathbb{R}^{m \times d}$, $\Theta \in \mathbb{R}^{d \times d}$, where the transformed viscous tensor is

$$\bar{D}_{ijps} : (\bar{W}; \Theta) \mapsto \det(\Theta) D(\bar{W})_{ikpl} \Theta_{sl}^{-1} \Theta_{jk}^{-1}. \quad (10)$$

2.3. Interior penalty discontinuous Galerkin discretization of transformed conservation law

We use an IPDG method [1, 2, 23, 24] to discretize the transformed conservation law (5). Let $\mathcal{E}_{h,q}$ represent a discretization of the reference domain Ω_0 into non-overlapping computational elements, where h is the mesh size parameter and each element $K \in \mathcal{E}_{h,q}$ is generated by a q -degree polynomial mapping applied to a parent element $\Omega_\square \subset \mathbb{R}^d$; i.e., $K = \mathcal{Q}_q^K(\Omega_\square)$ where $\mathcal{Q}_q^K \in [\mathcal{P}_q(\Omega_\square)]^d$ and $\mathcal{P}_a(\mathcal{S})$ is the space of polynomial functions of degree at most a over the domain $\mathcal{S} \subset \mathbb{R}^d$. To establish the finite-dimensional IPDG formulation, we first convert the second-order transformed conservation law into a system of first-order equations

$$\bar{\nabla} \cdot \bar{F}_{\text{inv}}(\bar{U}; G) - \bar{\nabla} \cdot \bar{\sigma} = \bar{S}(\bar{U}, \bar{\nabla} \bar{U}; G), \quad \bar{\sigma} = \bar{D}(\bar{U}; G) : \bar{\nabla} \bar{U}, \quad (11)$$

where $\bar{\sigma} : \Omega_0 \rightarrow \mathbb{R}^{m \times d}$, $\bar{\sigma} : X \mapsto \bar{\sigma}(X)$ is an auxiliary variable that represents the transformed viscous flux. Next, we introduce two finite-dimensional discontinuous piecewise polynomial approximation spaces

$$\begin{aligned}\mathcal{V}_{h,q,s} &= \{v \in [L^2(\Omega_0)]^m \mid v|_K \circ [\mathcal{Q}_q^K]^{-1} \in [\mathcal{P}_{p(K)+s}(\Omega_\square)]^m, \forall K \in \mathcal{E}_{h,q}\}, \\ \mathcal{T}_{h,q,s} &= \{v \in [L^2(\Omega_0)]^{m \times d} \mid v|_K \circ [\mathcal{Q}_q^K]^{-1} \in [\mathcal{P}_{p(K)+s}(\Omega_\square)]^{m \times d}, \forall K \in \mathcal{E}_{h,q}\},\end{aligned}\quad (12)$$

where $\mathcal{V}_{h,q,s}$ is the trial space for the flow solution (\bar{U}), $\mathcal{T}_{h,q,s}$ is the trial space for the viscous flux ($\bar{\sigma}$), and $p : \mathcal{E}_{h,q} \rightarrow \mathbb{N}$ is the distribution of polynomial approximation degree over the mesh. Next, we define the space of globally continuous piecewise polynomials of degree q associated with the mesh $\mathcal{E}_{h,q}$ as

$$\mathcal{W}_{h,q} = \{v \in H^1(\Omega_0) \mid v|_K \circ [\mathcal{Q}_q^K]^{-1} \in \mathcal{P}_q(\Omega_\square), \forall K \in \mathcal{E}_{h,q}\}, \quad (13)$$

and discretize the domain mapping \mathcal{G} with the corresponding vector-valued space $[\mathcal{W}_{h,q}]^d$. From these definitions, the primal weighted residual of the IPDG method is $r_{h,q,\delta,\Delta}(\cdot, \cdot; \cdot, \rho) : \mathcal{V}_{h,q,\Delta} \times \mathcal{V}_{h,q,\delta} \times [\mathcal{W}_{h,q}]^d \rightarrow \mathbb{R}$ with

$$r_{h,q,\delta,\Delta} : (\bar{\psi}_h, \bar{W}_h; \mathcal{G}_h, \rho) \mapsto \sum_{K \in \mathcal{E}_{h,q}} \rho(K) r_{h,q,\delta,\Delta}^K(\bar{\psi}_h, \bar{W}_h, \mathcal{G}_h), \quad (14)$$

given the trial enrichment $\delta \geq 0$, test enrichment $\Delta \geq 0$, trial function $\bar{W}_h \in \mathcal{V}_{h,q,\delta}$, test function $\bar{\psi}_h \in \mathcal{V}_{h,q,\Delta}$, mapping $\mathcal{G}_h \in \mathcal{W}_{h,q}$, and elemental scaling function $\rho : \mathcal{E}_{h,q} \rightarrow \mathbb{R}_{\geq 0}$ that will be used in Section 3.5.3 to emphasize boundary layer features. The elemental residual, $r_{h,q,\delta,\Delta}^K : \mathcal{V}_{h,q,\Delta} \times \mathcal{V}_{h,q,\delta} \times [\mathcal{W}_{h,q}]^d \rightarrow \mathbb{R}$, is given by

$$\begin{aligned}r_{h,q,\delta,\Delta}^K : (\bar{\psi}_h, \bar{W}_h, \mathcal{G}_h) \mapsto & \int_{\partial K} \bar{\psi}_h^+ \cdot (\bar{\mathcal{H}}(\bar{W}_h^+, \bar{W}_h^-, N_h; \bar{\nabla} \mathcal{G}_h) - \hat{\sigma}(\bar{W}_h^+, \bar{W}_h^-, \bar{\nabla} \bar{W}_h^+, \bar{\nabla} \bar{W}_h^-; \bar{\nabla} \mathcal{G}_h) N_h) dS \\ & - \frac{1}{2} \int_{\partial K} (\nabla \bar{\psi}_h^+ : \bar{D}(\bar{W}_h^+; \bar{\nabla} \mathcal{G}_h)) : [(\bar{W}_h^+ - \bar{W}_h^-) \otimes N_h] dS \\ & - \int_K \bar{\nabla} \bar{\psi}_h : (\bar{F}_{\text{inv}}(\bar{W}_h; \bar{\nabla} \mathcal{G}_h) - \bar{D}(\bar{W}_h; \bar{\nabla} \mathcal{G}_h) : \bar{\nabla} \bar{W}_h) dV \\ & - \int_K \bar{\psi}_h \cdot \bar{S}(\bar{W}_h, \bar{\nabla} \bar{W}_h; \bar{\nabla} \mathcal{G}_h) dV.\end{aligned}\quad (15)$$

where $N_h : \partial K \rightarrow \mathbb{R}^d$ is the unit outward normal to element $K \in \mathcal{E}_{h,q}$, and $\bar{W}_h^+(\bar{W}_h^-)$ denotes the interior (exterior) trace of $\bar{W}_h \in \mathcal{V}_{h,q,\delta}$ to the element, and $\bar{\mathcal{H}} : \mathbb{R}^m \times \mathbb{R}^m \times \mathbb{R}^d \times \mathbb{R}^{d \times d} \rightarrow \mathbb{R}^m$ is the transformed inviscid numerical flux function [54]. The transformed viscous numerical flux function, $\hat{\sigma} : \mathbb{R}^m \times \mathbb{R}^m \times \mathbb{R}^{m \times d} \times \mathbb{R}^{m \times d} \times \mathbb{R}^{d \times d} \rightarrow \mathbb{R}^{m \times d}$, is defined using the approach in [23]

$$\hat{\sigma} : (\bar{W}_h^+, \bar{W}_h^-, \bar{\nabla} \bar{W}_h^+, \bar{\nabla} \bar{W}_h^-; \bar{\nabla} \mathcal{G}_h) \rightarrow \{ \bar{D}(\bar{W}_h; \bar{\nabla} \mathcal{G}_h) \bar{\nabla} \bar{W}_h \} - \delta_{\text{IP}}(\bar{W}_h^+, \bar{W}_h^-; \bar{\nabla} \mathcal{G}_h), \quad (16)$$

where $\{v\} = (v^+ + v^-)/2$ is the average operator and $\delta_{\text{IP}} : \mathbb{R}^m \times \mathbb{R}^m \times \mathbb{R}^{d \times d} \rightarrow \mathbb{R}^{m \times d}$ is the penalty term

$$\delta_{\text{IP}}|_{\partial K \cap \partial K'} : (\bar{W}_h^+, \bar{W}_h^-; \bar{\nabla} \mathcal{G}_h) \mapsto C_{\text{IP}} \frac{\max\{p(K), p(K')\} + \delta}{h} \{ \bar{D}(\bar{W}_h; \bar{\nabla} \mathcal{G}_h) \} : [(\bar{W}_h^+ - \bar{W}_h^-) \otimes N_h], \quad (17)$$

with $h = \min\{|K|, |K'|\}/|\partial K \cap \partial K'|$ being the linear mesh size associated with the face $\bar{K} \cap \bar{K}'$ and N_h is the outward unit normal to element K , and $C_{\text{IP}} \in \mathbb{R}_{>0}$ is a user-defined stabilization parameter. On boundary faces, i.e., $\partial K \cap \partial \Omega_0$, the inviscid and viscous numerical fluxes are modified to enforce the appropriate boundary condition.

Finally, we introduce a basis for the test space $(\mathcal{V}_{h,q,\Delta})$, trial space $(\mathcal{V}_{h,q,\delta})$, and domain mapping space $([\mathcal{W}_{h,q}]^d)$ to reduce the weak formulation in residual form to a system of nonlinear algebraic equations in residual form. In the case where $\delta = \Delta = 0$ and $\rho = \mathbb{1}$ is the one function, $\mathbb{1} : \mathcal{E}_{h,q} \rightarrow \{1\}$ with $\mathbb{1} : K \mapsto 1$, we denote the algebraic residual

$$\mathbf{r} : \mathbb{R}^{N_u} \times \mathbb{R}^{N_x} \rightarrow \mathbb{R}^{N_u}, \quad \mathbf{r} : (\mathbf{u}, \mathbf{x}) \mapsto \mathbf{r}(\mathbf{u}, \mathbf{x}), \quad (18)$$

where $N_{\mathbf{u}} = \dim \mathcal{V}_{h,q,0}$ and $N_{\mathbf{x}} = \dim([\mathcal{W}_{h,q}]^d)$, $\mathbf{u} \in \mathbb{R}^{N_{\mathbf{u}}}$ are the coefficients of the flow solution (\bar{U}_h), and $\mathbf{x} \in \mathbb{R}^{N_{\mathbf{x}}}$ are the coefficients of the domain mapping (\mathcal{G}_h). Assuming a nodal basis is used for the continuous space $\mathcal{W}_{h,q}$, the coefficients \mathbf{x} are equal to nodal coordinates in the physical domain. In this notation, a standard IPDG discretization (algebraic form) reads: given $\mathbf{x} \in \mathbb{R}^{N_{\mathbf{x}}}$ (from mesh generation), find $\mathbf{u} \in \mathbb{R}^{N_{\mathbf{u}}}$ such that $\mathbf{r}(\mathbf{u}, \mathbf{x}) = \mathbf{0}$. In the case where $\delta = \Delta = 1$ and $\rho = \mathbb{1}$, we denote the algebraic residual

$$\tilde{\mathbf{r}} : \mathbb{R}^{\tilde{N}_{\mathbf{u}}} \times \mathbb{R}^{N_{\mathbf{x}}} \rightarrow \mathbb{R}^{\tilde{N}_{\mathbf{u}}}, \quad \tilde{\mathbf{r}} : (\tilde{\mathbf{u}}, \mathbf{x}) \mapsto \tilde{\mathbf{r}}(\tilde{\mathbf{u}}, \mathbf{x}), \quad (19)$$

where $\tilde{N}_{\mathbf{u}} = \dim \mathcal{V}_{h,q,1}$ and $\tilde{\mathbf{u}} \in \mathbb{R}^{\tilde{N}_{\mathbf{u}}}$ are the coefficients of the flow solution in the finer trial space ($\delta = 1$). The fine-space residual $\tilde{\mathbf{r}}$ is the result of a single level of global p -refinement applied to the coarse-space residual \mathbf{r} , and will be used to drive dual-weighted residual-based p -adaptivity. Finally, in the case where $\delta = 0$ and $\Delta > 0$, we denote the algebraic residual

$$\mathbf{R}_{\rho} : \mathbb{R}^{N_{\mathbf{u}}} \times \mathbb{R}^{N_{\mathbf{x}}} \rightarrow \mathbb{R}^{\hat{N}_{\mathbf{u}}}, \quad \mathbf{R}_{\rho} : (\mathbf{u}, \mathbf{x}) \mapsto \mathbf{R}_{\rho}(\mathbf{u}, \mathbf{x}), \quad (20)$$

where $\hat{N}_{\mathbf{u}} = \dim \mathcal{V}_{h,q,\Delta}$. For brevity, we denote the special case $\rho = \mathbb{1}$, as

$$\mathbf{R} : \mathbb{R}^{N_{\mathbf{u}}} \times \mathbb{R}^{N_{\mathbf{x}}} \rightarrow \mathbb{R}^{\hat{N}_{\mathbf{u}}}, \quad \mathbf{R} : (\mathbf{u}, \mathbf{x}) \mapsto \mathbf{R}_{\mathbb{1}}(\mathbf{u}, \mathbf{x}). \quad (21)$$

This enriched residual has a larger test space than trial space, and will be used to formulate the implicit shock tracking method (Section 3).

Remark 1. *Due to the discontinuous test function, the IPDG method requires each element residual be zero. Therefore, the elemental scaling function ρ does not alter the solution provided it is non-zero in all elements. As such, typically it is taken to be unity, i.e., $\rho = \mathbb{1}$. However, ρ changes the relative scaling of the element residuals, which alters local minima of the enriched residual. Therefore, ρ plays an important role in implicit shock tracking, which minimizes the enriched residual to compress elements into steep features (Section 3). We introduce a simple strategy to define ρ to emphasize boundary layer features (Section 3.5.3) and demonstrate its importance (Section 4.2.2).*

Remark 2. *The transformed viscous tensor \bar{D} is required by the IPDG method in (15). However, the viscous tensor only appears in contraction operations with either a trial or test function. By appealing to (9), any contraction involving the transformed viscous tensor can be written as an evaluation of the transformed viscous flux (F_{visc}), which can in turn be written as an evaluation of the physical viscous flux (F_{visc}) using (8). This approach is convenient as it only requires a single, efficient implementation of the viscous flux in (1) and transformations in (8) to implement the IPDG scheme.*

Remark 3. *There are two obvious ways to compute quantities of interest that depend on the viscous flux $F_{\text{visc}}(\bar{U}_h, \nabla \bar{U}_h; \bar{\nabla} \mathcal{G}_h)$, where $\bar{U}_h \in \mathcal{V}_{h,q,\delta}$ satisfies $r_{h,q,0,0}(\bar{\psi}_h, \bar{U}_h; \mathcal{G}_h, \rho) = 0$ for all $\bar{\psi}_h \in \mathcal{V}_{h,q,0}$ given \mathcal{G}_h and ρ . The first option is, for any $X \in \Omega_0$, to evaluate $F_{\text{visc}}(\bar{U}_h(X), \nabla \bar{U}_h(X); \bar{\nabla} \mathcal{G}_h(X))$, where $\nabla \bar{U}_h(X)$ is computed by direct differentiation of the polynomial basis used to represent $\mathcal{V}_{h,q,\delta}$ over each element (using the same coefficients defining \bar{U}). The other option appeals to the first-order form of the conservation law (11) and uses the viscous flux that is consistent with the IPDG discretization, i.e., given the solution $\bar{U}_h \in \mathcal{V}_{h,q,\delta}$, find $\bar{\sigma}_h \in \mathcal{T}_{h,q,\delta}$ such that*

$$\int_K \bar{\tau}_h : (\bar{\sigma}_h - \bar{D}(\bar{U}_h) : \bar{\nabla} \bar{U}_h) dV + \int_{\partial K} (\bar{\tau}^+ : \bar{D}(\bar{U}_h^+) : [(\bar{U}_h^+ - \bar{U}_h^-) \otimes N_h]) dS = 0 \quad (22)$$

holds for all $\bar{\tau}_h \in \mathcal{T}_{h,q,\delta}$ and $K \in \mathcal{E}_{h,q}$. Then, the viscous flux at $X \in \Omega_0$ is approximated as $\bar{\sigma}_h(X)$. In Section 4.2.2 we show the second option, i.e., the lifted viscous flux, provides more accurate and less oscillatory quantities of interest, which is consistent with previous work showing this choice leads to dual-consistent evaluation of output functionals and hence to superconvergence of the output [34, 22].

2.4. Error estimation and p -adaptivity

We close this section with a review of elemental error estimation and p -adaptivity, which will be used in Section 3 to formulate the proposed rp -adaptive implicit shock tracking method. First, we introduce a

sequence of polynomial degree distributions, $\{p_j\}_{j=0}^n$ with $p_j : \mathcal{E}_{h,q} \rightarrow \mathbb{N}$. The function spaces in (12) based on this sequence of polynomial distributions are denoted $\mathcal{V}_{h,q,s}^{(j)}$ and $\mathcal{T}_{h,q,s}^{(j)}$, respectively. Furthermore, the algebraic residuals in (18)–(21) based on this sequence of polynomial distributions are similarly denoted $\mathbf{r}^{(j)} : \mathbb{R}^{N_{\mathbf{u}}^{(j)}} \times \mathbb{R}^{N_{\mathbf{x}}} \rightarrow \mathbb{R}^{N_{\mathbf{u}}^{(j)}}$, $\tilde{\mathbf{r}}^{(j)} : \mathbb{R}^{\tilde{N}_{\mathbf{u}}^{(j)}} \times \mathbb{R}^{N_{\mathbf{x}}} \rightarrow \mathbb{R}^{\tilde{N}_{\mathbf{u}}^{(j)}}$, $\mathbf{R}_p^{(j)} : \mathbb{R}^{N_{\mathbf{u}}^{(j)}} \times \mathbb{R}^{N_{\mathbf{x}}} \rightarrow \mathbb{R}^{\hat{N}_{\mathbf{u}}^{(j)}}$, and $\mathbf{R}^{(j)} : \mathbb{R}^{N_{\mathbf{u}}^{(j)}} \times \mathbb{R}^{N_{\mathbf{x}}} \rightarrow \mathbb{R}^{\hat{N}_{\mathbf{u}}^{(j)}}$, respectively, where $N_{\mathbf{u}}^{(j)} = \dim \mathcal{V}_{h,q,0}^{(j)}$, $\tilde{N}_{\mathbf{u}}^{(j)} = \dim \tilde{\mathcal{V}}_{h,q,1}^{(j)}$, and $\hat{N}_{\mathbf{u}}^{(j)} = \dim \mathcal{V}_{h,q,\Delta}^{(j)}$.

The initial polynomial degree distribution, p_0 , is usually chosen to be constant across the mesh. Each p -adaptive iteration locally increases the polynomial degree from p_j to p_{j+1} based on the distribution of an elemental error indicator $s_j : \mathcal{E}_{h,q} \rightarrow \mathbb{R}_{\geq 0}$ as

$$p_{j+1} : K \mapsto \begin{cases} p_j(K) + 1, & s_j(K) > \tau \max_{K' \in \mathcal{E}_{h,q}} s_j(K') \\ p_j(K), & \text{otherwise,} \end{cases} \quad (23)$$

where $\tau > 0$ is a threshold used to identify which elements to refine. The error indicator is a constant scalar over each element of the mesh $\mathcal{E}_{h,q}$ that approximates some measure of the error between the discrete and true (\bar{U}) attributed to the element. It is used to identify the elements with the largest contribution to the overall error for p -refinement. In the following sections, we review three popular error indicators studied in the context of the proposed rp -adaptive method.

2.4.1. Enriched residual indicator

First, we consider the unweighted elemental enriched residual, $\hat{s}_j^{\text{uwr}} : \mathcal{E}_{h,q} \times \mathbb{R}^{N_{\mathbf{u}}^{(j)}} \times \mathbb{R}^{N_{\mathbf{x}}} \rightarrow \mathbb{R}_{\geq 0}$, defined as

$$\hat{s}_j^{\text{uwr}} : (K, \mathbf{u}, \mathbf{x}) \mapsto \left\| (\hat{\mathbf{P}}_K^{(j)})^T \mathbf{R}^{(j)}(\mathbf{u}, \mathbf{x}) \right\|_2, \quad (24)$$

where $\hat{\mathbf{P}}_K^{(j)} \in \mathbb{R}^{\hat{N}_{\mathbf{u}}^{(j)} \times \hat{N}_{\mathbf{u}}^{(j),K}}$ is the assembly operator that maps the local degrees of freedom associated with element $K \in \mathcal{E}_{h,q}$ to the corresponding global degrees of freedom for the test space $\hat{\mathcal{V}}_K^{(j)}$, and the transpose restricts global degrees of freedom to the degrees of freedom associated with element K . This error indicator is less popular than dual-weighted variants [6, 5, 18] (Section 2.4.2); however, it is natural to use in the context of implicit shock tracking because it is used to define the shock tracking objective function (Section 3.1).

2.4.2. Dual-weighted residual indicator

Next, we consider dual-weighted elemental residual indicator [6, 5, 18], $\hat{s}_j^{\text{dwr}} : \mathcal{E}_{h,q} \times \mathbb{R}^{N_{\mathbf{u}}^{(j)}} \times \mathbb{R}^{N_{\mathbf{x}}} \rightarrow \mathbb{R}_{\geq 0}$, defined as

$$\hat{s}_j^{\text{dwr}} : (K, \mathbf{u}, \mathbf{x}) \mapsto \left| \left[(\hat{\mathbf{Q}}_K^{(j)})^T \boldsymbol{\Psi}^{(j)}(\mathbf{u}, \mathbf{x}) \right] \cdot (\hat{\mathbf{Q}}_K^{(j)})^T \mathbf{R}^{(j)}(\mathbf{u}, \mathbf{x}) \right| \quad (25)$$

where the dual variable $\boldsymbol{\Psi}^{(j)} : \mathbb{R}^{N_{\mathbf{u}}^{(j)}} \times \mathbb{R}^{N_{\mathbf{x}}} \rightarrow \mathbb{R}^{\hat{N}_{\mathbf{u}}^{(j)}}$ is implicitly defined as the solution of the fine-space adjoint equations, i.e.,

$$\boldsymbol{\Psi}^{(j)} : (\mathbf{u}, \mathbf{x}) \mapsto \left[\frac{\partial \tilde{\mathbf{r}}^{(j)}}{\partial \tilde{\mathbf{u}}}(\tilde{\mathbf{Q}}^{(j)} \mathbf{u}, \mathbf{x}) \right]^{-T} \frac{\partial \tilde{J}^{(j)}}{\partial \tilde{\mathbf{u}}}(\tilde{\mathbf{Q}}^{(j)} \mathbf{u}, \mathbf{x})^T \quad (26)$$

and $\tilde{\mathbf{Q}}^{(j)} \in \mathbb{R}^{\tilde{N}_{\mathbf{u}}^{(j)} \times N_{\mathbf{u}}^{(j)}}$ is a discrete prolongation operator that maps the coarse-space ($\delta = 0$) coefficients $\mathbf{u} \in \mathbb{R}^{N_{\mathbf{u}}^{(j)}}$ to the fine-space ($\delta = 1$) coefficients $\tilde{\mathbf{u}} \in \mathbb{R}^{\tilde{N}_{\mathbf{u}}^{(j)}}$ that reproduces the same function over Ω_0 . Furthermore, $\tilde{J}^{(j)} : \mathbb{R}^{\tilde{N}_{\mathbf{u}}^{(j)}} \times \mathbb{R}^{N_{\mathbf{x}}} \rightarrow \mathbb{R}$ with $\tilde{J}^{(j)} : (\tilde{\mathbf{u}}, \mathbf{x}) \mapsto \tilde{J}^{(j)}(\tilde{\mathbf{u}}, \mathbf{x})$ is the algebraic form (fine-space, $\delta = 1$) of the continuous-level quantity of interest

$$\mathcal{J} : (\bar{U}, \mathcal{G}) \mapsto \int_{\mathcal{G}(\Omega_0)} q_v(\bar{U}; \mathcal{G}) dV + \int_{\mathcal{G}(\partial\Omega_0)} q_b(\bar{U}; \mathcal{G}) dS, \quad (27)$$

based on the trial space $\mathcal{V}_{h,q,1}^{(j)}$, where $q_v(\bar{U}, \mathcal{G})$ is the volumetric quantity of interest and $q_b(\bar{U}, \mathcal{G})$ is the boundary quantity of interest. In this work, we take $q_v = 0$ and q_b is the drag (Section 4.2.1) or heat flux (Section 4.2.6) over a relevant boundary. This is a popular error indicator because the sum of \hat{s}_j^{dwr} across

all elements in the mesh provides an estimate of the error between the true quantity of interest $\mathcal{J}(\bar{U}, \mathcal{G})$ and the discrete approximate $\tilde{J}^{(j)}(\tilde{\mathbf{u}}, \mathbf{x})$ [49, 48, 18].

2.4.3. Feature-based indicator

Lastly, we consider a feature-based indicator, $\hat{s}_j^{\text{fbs}} : \mathcal{E}_{h,q} \times \mathbb{R}^{N_{\mathbf{u}}^{(j)}} \times \mathbb{R}^{N_{\mathbf{x}}} \rightarrow \mathbb{R}_{\geq 0}$, defined as

$$\hat{s}_j^{\text{fbs}} : (K, \mathbf{u}, \mathbf{x}) \mapsto \int_{\mathcal{G}(K)} \vartheta(\bar{U}, \mathcal{G}) dV, \quad (28)$$

where $\vartheta : \mathcal{V}_{h,q,0}^{(j)} \times [\mathcal{W}_{h,q}]^d \rightarrow \mathbb{R}$ is a relevant volumetric sensor. In this work, we use the gradient of the solution vector $\vartheta(\bar{U}, \mathcal{G}) = \|\bar{\nabla} \bar{U} \cdot (\bar{\nabla} \mathcal{G})^{-1}\|$. Such sensors detect regions of significant physical change in the state and can selectively identify shocks and boundary layers. However, the sensor does not diminish as resolution increases, which can cause refinement to be incorrectly focused and does not admit a natural termination criteria.

3. A p -adaptive high-order implicit shock tracking method for viscous conservation laws

In this section, we embed the HOIST method [51, 53, 26] in a p -adaptivity setting (Section 3.1) and recall the sequential quadratic programming solver [26] (Section 3.2). Finally, we introduce modifications to the HOIST formulation and solver necessary to fully resolve shock and boundary layers in viscous conservation law solutions (Section 3.5) and summarize the complete algorithm (Section 3.6).

3.1. Optimization formulation

The HOIST method treats both the discrete solution of the conservation law (\mathbf{u}) and the nodal coordinates of the mesh (\mathbf{x}) as unknowns, which are determined as the solution of a PDE-constrained optimization problem. In the viscous setting, we seek nodal coordinates that cause mesh elements to compress into steep features such as shocks and boundary layers, and flow variables that satisfy the IPDG equations with $\delta = \Delta = 0$ on the tailored mesh. On the j th p -adaptivity iteration, the optimization problem is formulated as

$$\left(\mathbf{u}_{\star}^{(j)}(\Xi), \mathbf{y}_{\star}^{(j)}(\Xi) \right) := \arg \min_{\mathbf{u} \in \mathbb{R}^{N_{\mathbf{u}}}, \mathbf{y} \in \mathbb{R}^{N_{\mathbf{y}}}} f^{(j)}(\mathbf{u}, \mathbf{y}; \Xi) \quad \text{subject to:} \quad \mathbf{r}^{(j)}(\mathbf{u}, \phi(\mathbf{y}); \Xi) = \mathbf{0}, \quad (29)$$

where $f^{(j)} : \mathbb{R}^{N_{\mathbf{u}}} \times \mathbb{R}^{N_{\mathbf{y}}} \rightarrow \mathbb{R}$ is the objective function, $\mathbf{y} \in \mathbb{R}^{N_{\mathbf{y}}}$ are the unconstrained mesh degrees of freedom, $\phi : \mathbb{R}^{N_{\mathbf{y}}} \rightarrow \mathbb{R}^{N_{\mathbf{x}}}$ is a parametrization of the nodal coordinates that ensures $\mathbf{x} = \phi(\mathbf{y})$ represents a physical mesh where all nodes remain on their original boundaries for any $\mathbf{y} \in \mathbb{R}^{N_{\mathbf{y}}}$ [54, 26, 41], and $\Xi \in \mathbb{R}$ is a continuation parameter. Continuation (Section 3.3 and 3.5.7) will be used as an ‘‘outer loop’’ around the optimization problem in (29) to facilitate robust initialization and convergence. The r -adapted mesh coordinates are reconstructed from the unconstrained degrees of freedom as $\mathbf{x}_{\star}^{(j)} = \phi(\mathbf{y}_{\star}^{(j)}(\Xi))$. The objective function is composed of two terms as

$$f^{(j)} : (\mathbf{u}, \mathbf{y}; \Xi) \mapsto f_{\text{err}}^{(j)}(\mathbf{u}, \mathbf{y}; \Xi) + \kappa^2 f_{\text{msh}}(\mathbf{y}), \quad (30)$$

which balances alignment of the mesh with compression of the mesh into steep features and the quality of mesh. The mesh alignment term, $f_{\text{err}}^{(j)} : \mathbb{R}^{N_{\mathbf{u}}} \times \mathbb{R}^{N_{\mathbf{y}}} \rightarrow \mathbb{R}_{>0}$, is taken to be the norm of enriched DG residual

$$f_{\text{err}}^{(j)} : (\mathbf{u}, \mathbf{y}; \Xi) \mapsto \frac{1}{2} \left\| \mathbf{R}_{\rho}^{(j)}(\mathbf{u}, \phi(\mathbf{y}); \Xi) \right\|_2^2, \quad (31)$$

where $\rho : \Omega_0 \rightarrow \mathbb{R}_{\geq 0}$ is an element scaling defined in Section 2.3 that will be used to emphasize the boundary layer (Section 3.5.3). The mesh distortion term, $f_{\text{msh}} : \mathbb{R}^{N_{\mathbf{y}}} \rightarrow \mathbb{R}_{>0}$, is defined as

$$f_{\text{msh}} : \mathbf{y} \mapsto \frac{1}{2} \left\| \mathbf{R}_{\text{msh}}(\phi(\mathbf{y})) \right\|_2^2, \quad (32)$$

where $\mathbf{R}_{\text{msh}} : \mathbb{R}^{N_{\mathbf{x}}} \rightarrow \mathbb{R}_{>0}^{|\mathcal{E}_{h,q}|}$ is the elemental mesh distortion defined in [53], and $\kappa \in \mathbb{R}_{>0}$ is the mesh quality penalty parameter (Section 3.5.2). The objective function can be written as the two-norm of a residual function as

$$f^{(j)}(\mathbf{u}, \mathbf{y}; \Xi) = \frac{1}{2} \mathbf{F}^{(j)}(\mathbf{u}, \mathbf{y}; \Xi)^T \mathbf{F}^{(j)}(\mathbf{u}, \mathbf{y}; \Xi), \quad \mathbf{F}^{(j)} : (\mathbf{u}, \mathbf{y}; \Xi) \mapsto \begin{bmatrix} \mathbf{R}_{\rho}^{(j)}(\mathbf{u}, \phi(\mathbf{y}); \Xi) \\ \mathbf{R}_{\text{msh}}^{(j)}(\phi(\mathbf{y})) \end{bmatrix}, \quad (33)$$

where $\mathbf{F}^{(j)} : \mathbb{R}^{N_{\mathbf{u}}} \times \mathbb{R}^{N_{\mathbf{y}}} \rightarrow \mathbb{R}^{\hat{N}_{\mathbf{u}}^{(j)} + |\mathcal{E}_{h,q}|}$ is the residual, which allows for a Levenberg–Marquardt approximation to its Hessian (Section 3.2).

3.2. Sequential quadratic programming method

To solve the system in (29), we adapt the full-space sequential quadratic programming (SQP) method developed in [54, 26] that simultaneously drives \mathbf{u} and \mathbf{y} to their optimal values. The SQP solver defines a sequence of iterations $\{\mathbf{z}_0^{(j)}(\Xi), \mathbf{z}_1^{(j)}(\Xi), \dots\}$, where each iterate contains both the flow and mesh degrees of freedom, i.e., $\mathbf{z}_k^{(j)}(\Xi) = (\mathbf{u}_k^{(j)}(\Xi), \mathbf{y}_k^{(j)}(\Xi))$ that converges to the solution of (29): $\mathbf{z}_k^{(j)}(\Xi) \rightarrow (\mathbf{u}_\star^{(j)}(\Xi), \mathbf{y}_\star^{(j)}(\Xi))$. The starting point $\mathbf{z}_0^{(j)}(\Xi) = (\mathbf{u}_0^{(j)}(\Xi), \mathbf{y}_0^{(j)}(\Xi))$ is provided by the user, continuation, or p -adaptation strategy, and the SQP update is

$$\mathbf{z}_{k+1}^{(j)}(\Xi) = \chi_k^{(j)}(\tilde{\mathbf{z}}_{k+1}^{(j)}(\Xi); \Xi), \quad \tilde{\mathbf{z}}_{k+1}^{(j)}(\Xi) = \mathbf{z}_k^{(j)}(\Xi) + \alpha_k^{(j)}(\Xi) \Delta \mathbf{z}_k^{(j)}(\Xi), \quad (34)$$

where $\chi_k^{(j)}(\cdot; \Xi) : \mathbb{R}^{N_{\mathbf{u}}^{(j)} + N_{\mathbf{y}}} \rightarrow \mathbb{R}^{N_{\mathbf{u}}^{(j)} + N_{\mathbf{y}}}$ is a step modification function used to enhance the robustness of the solver (Section 3.5.5). The search direction, $\Delta \mathbf{z}_k^{(j)}(\Xi) \in \mathbb{R}^{N_{\mathbf{u}}^{(j)} + N_{\mathbf{y}}}$, is defined as the solution of the following quadratic program:

$$\begin{aligned} & \underset{\Delta \mathbf{z} \in \mathbb{R}^{N_{\mathbf{u}}^{(j)} + N_{\mathbf{y}}}}{\text{minimize}} && \mathbf{g}_k^{(j)}(\Xi) \Delta \mathbf{z} + \frac{1}{2} \Delta \mathbf{z}^T \mathbf{B}_k^{(j)}(\Xi) \Delta \mathbf{z} \\ & \text{subject to} && \mathbf{r}_k^{(j)}(\Xi) + \mathbf{J}_k^{(j)}(\Xi) \Delta \mathbf{z} = \mathbf{0}, \end{aligned} \quad (35)$$

where $\mathbf{r}_k^{(j)}(\Xi) = \mathbf{r}^{(j)}(\mathbf{u}_k^{(j)}(\Xi), \phi(\mathbf{y}_k^{(j)}(\Xi)))$ is the constraint function evaluated at $\mathbf{z}_k^{(j)}$, the first-order terms are defined as

$$\begin{aligned} \mathbf{g}_k^{(j)}(\Xi) &= \begin{bmatrix} \partial_{\mathbf{u}} f^{(j)}(\mathbf{u}_k^{(j)}(\Xi), \mathbf{y}_k^{(j)}(\Xi); \Xi)^T \\ \partial_{\mathbf{y}} f^{(j)}(\mathbf{u}_k^{(j)}(\Xi), \mathbf{y}_k^{(j)}(\Xi); \Xi)^T \end{bmatrix}, \\ \mathbf{J}_k^{(j)}(\Xi) &= \begin{bmatrix} \partial_{\mathbf{u}} \mathbf{r}^{(j)}(\mathbf{u}_k^{(j)}(\Xi), \mathbf{y}_k^{(j)}(\Xi); \Xi) & \partial_{\mathbf{y}} \mathbf{r}^{(j)}(\mathbf{u}_k^{(j)}(\Xi), \mathbf{y}_k^{(j)}(\Xi); \Xi) \end{bmatrix}. \end{aligned} \quad (36)$$

The second-order term uses the following Levenberg–Marquardt Hessian approximation

$$\mathbf{B}_k^{(j)}(\Xi) = \begin{bmatrix} \mathbf{B}_{\mathbf{u}\mathbf{u},k}^{(j)}(\Xi) & \mathbf{B}_{\mathbf{u}\mathbf{y},k}^{(j)}(\Xi) \\ \mathbf{B}_{\mathbf{u}\mathbf{y},k}^{(j)}(\Xi)^T & \mathbf{B}_{\mathbf{y}\mathbf{y},k}^{(j)}(\Xi) \end{bmatrix}, \quad (37)$$

where the individual terms are

$$\begin{aligned} \mathbf{B}_{\mathbf{u}\mathbf{u},k}^{(j)}(\Xi) &= \partial_{\mathbf{u}} \mathbf{F}^{(j)}(\mathbf{u}_k^{(j)}(\Xi), \mathbf{y}_k^{(j)}(\Xi); \Xi)^T \partial_{\mathbf{u}} \mathbf{F}^{(j)}(\mathbf{u}_k^{(j)}(\Xi), \mathbf{y}_k^{(j)}(\Xi); \Xi), \\ \mathbf{B}_{\mathbf{u}\mathbf{y},k}^{(j)}(\Xi) &= \partial_{\mathbf{u}} \mathbf{F}^{(j)}(\mathbf{u}_k^{(j)}(\Xi), \mathbf{y}_k^{(j)}(\Xi); \Xi)^T \partial_{\mathbf{y}} \mathbf{F}^{(j)}(\mathbf{u}_k^{(j)}(\Xi), \mathbf{y}_k^{(j)}(\Xi); \Xi), \\ \mathbf{B}_{\mathbf{y}\mathbf{y},k}^{(j)}(\Xi) &= \partial_{\mathbf{y}} \mathbf{F}^{(j)}(\mathbf{u}_k^{(j)}(\Xi), \mathbf{y}_k^{(j)}(\Xi); \Xi)^T \partial_{\mathbf{y}} \mathbf{F}^{(j)}(\mathbf{u}_k^{(j)}(\Xi), \mathbf{y}_k^{(j)}(\Xi); \Xi) + \gamma_k^{(j)}(\Xi) \mathbf{D}_k^{(j)}(\Xi), \end{aligned} \quad (38)$$

and $\mathbf{D}_k^{(j)}(\Xi) \in \mathbb{R}^{N_{\mathbf{y}} \times N_{\mathbf{y}}}$ is a regularization matrix and $\gamma_k^{(j)}(\Xi) \in \mathbb{R}_{\geq 0}$ is a regularization parameter (Section 3.5.6) applied only to the mesh component of the Hessian approximation. Finally, the step length, $\alpha_k^{(j)}(\Xi) \in (0, \hat{\alpha}_k^{(j)}]$, is obtained from a backtracking line search [40] on the ℓ_1 merit function of (29) with penalty parameter chosen according to [26]. The maximum step length $\hat{\alpha}_k^{(j)}(\Xi) \in (0, 1]$ is chosen to ensure the next iteration remains physical (Section 3.5.4). The quadratic program in (35) can be recast as a linear

system of equations by appealing to the first-order optimality conditions; for additional detail see [26].

3.3. Continuation

The continuation parameter, Ξ , is used to improve the robustness of the shock tracking solver (Section 3.2) and avoid spurious features (such as carbuncles [42, 44]) by defining a sequence of optimization problems, each one with an reasonable starting point, ending with the optimization problem of interest ($\Xi = \Xi_*$). Continuation is only required *prior* to adaption of the polynomial degree ($j = 0$), i.e., when the flow and grid are far from convergence. To this end, we introduce a sequence $\{\Xi_1, \Xi_2, \dots, \Xi_c = \Xi_*\}$, where c is the number of continuation steps, and initialize the optimization problem in (29) for $\Xi = \Xi_i$ with

$$\mathbf{u}_0^{(0)}(\Xi_i) := \mathbf{u}_*^{(0)}(\Xi_{i-1}), \quad \mathbf{y}_0^{(0)}(\Xi_i) := \mathbf{y}_*^{(0)}(\Xi_{i-1}) \quad (39)$$

for $i = 2, \dots, c$. The initial guess for (29) with $\Xi = \Xi_1$ comes from a shock capturing simulation (initialization of \mathbf{u}) on a shock-agnostic mesh obtained from mesh generation (initialization of \mathbf{y}). Once the continuation process is complete, the solution $(\mathbf{u}_*^{(0)}(\Xi_*), \mathbf{y}_*^{(0)}(\Xi_*))$ is available and represents a purely r -adapted solution.

3.4. p -Adaptivity

Next, we introduce p -adaptivity to further improve the r -adapted approximation. Given the solution at the final continuation parameter $\Xi = \Xi_*$ of the j th p -adaption iteration, i.e., $(\mathbf{u}_*^{(j)}(\Xi_*), \mathbf{y}_*^{(j)}(\Xi_*))$, we locally increase the polynomial degree according to (23) using the indicator

$$s_j : K \mapsto \hat{s}_j(K, \mathbf{u}_*^{(j)}(\Xi_*), \mathbf{x}_*^{(j)}(\Xi_*)), \quad (40)$$

where \hat{s}_j is any of the indicators introduced in Sections 2.4.1-2.4.3, to obtain the new polynomial degree distribution p_{j+1} . The optimization problem at the new refinement level, i.e., $j \leftarrow j + 1$ and $\Xi = \Xi_*$, is initialized from prolongation of the previous solution $\mathbf{u}_*^{(j)}(\Xi_*)$ into the finer space to define $\mathbf{u}_0^{(j+1)}(\Xi_*)$, and the mesh is directly transferred, i.e., $\mathbf{y}_0^{(j+1)}(\Xi_*) = \mathbf{y}_*^{(j)}(\Xi_*)$. From this starting point, the solver in Section 3.2 is applied to obtain $\mathbf{u}_*^{(j+1)}(\Xi_*)$ and $\mathbf{y}_*^{(j+1)}(\Xi_*)$. The p -adaption iterations are terminated at iteration $j = J$, where one of the following conditions are met

$$\left\| \mathbf{R}^{(J)}(\mathbf{u}_*^{(J)}(\Xi_*), \phi(\mathbf{y}_*^{(J)}(\Xi_*)); \Xi_*) \right\| \leq \hat{\epsilon} \quad \text{or} \quad J = J_{\max}, \quad (41)$$

where $\hat{\epsilon} > 0$ and $J_{\max} \in \mathbb{N}$ are user-defined parameters. The final rp -adapted flow solution is $\mathbf{u}_*^{(J)}(\Xi_*)$ on the transformed mesh defined by the nodal coordinates $\phi(\mathbf{y}_*^{(J)}(\Xi_*))$.

3.5. Solver details tailored to viscous flows

The exposition in Section 3.1-3.4 provides an overview of the HOIST method initially introduced in [54, 26] enriched with continuation in [25] and p -adaptivity in [15]. The remainder of this section completes the missing algorithmic details necessary for the HOIST method to act as an aggressive r -adaptive method to compress elements into steep viscous flow features.

3.5.1. Enrichment degree

The enriched residual is used to defined the implicit shock tracking objective function in (31); however, the enrichment degree Δ , defined in (20)-(21), has been unspecified to this point. The choice $\Delta = 1$ has been shown to lead to accurate and robust shock tracking for inviscid flows across a number of applications [54, 52, 26, 25, 39]. However, for viscous problems, $\Delta = 1$ leads to suboptimal meshes and insufficient boundary layer resolution (Section 4.2.4), especially when the solution is severely underresolved. On the other hand, $\Delta = 2$ has led to reliable and aggressive r -adaptivity to both viscous shocks and boundary layers for all problems considered in this work.

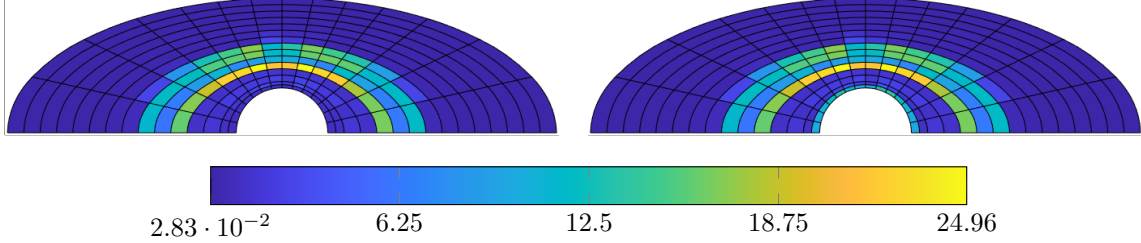


Figure 1: Elementwise magnitude of the enriched DG residual ($\Delta = 2$) for $M_\infty = 5$, $\text{Re} = 10^3$ hypersonic flow over a cylinder (isothermal wall) without (*left*) and with (*right*) boundary layer scaling ($\lambda = 10$).

3.5.2. Choice of mesh penalty parameter

For inviscid problems, κ is adapted throughout the iterations to ensure the tracking and mesh quality terms remain in balance [26]. However, in the viscous setting, our goal is to highly distort the elements to compress them into steep features, e.g., viscous shocks and boundary layers, which means $f_{\text{msh}}(\mathbf{y})$ will inevitably become large. Therefore, we choose κ to be a fixed, small, non-zero number (we take $\kappa = 10^{-6}$ in this work). This ensures that $\kappa^2 f_{\text{msh}}(\mathbf{y})$ will blow up if an inverted mesh is encountered and cause the line search to decrease the step length. However, for non-inverted meshes, the tracking term f_{err} will dominate.

3.5.3. Residual scaling to emphasize boundary layers

Implicit shock tracking methods prioritize stronger transitions over weaker ones, in the sense that many more SQP iterations are required to track weak transitions than strong ones, owing to the residual-based objective function [26]. For viscous flows, particularly in the hypersonic regime, shock waves are much stronger transitions than boundary layers. This is not typically a problem for standard DG discretizations that seek a root of $\mathbf{r}(\cdot, \mathbf{x})$ on a given mesh $\mathbf{x} \in \mathbb{R}^{N_x}$ because the residual on each element is driven to zero regardless of its initial magnitude; however, implicit shock tracking methods are minimum-residual methods whose solutions are highly dependent on the scaling of the residual. Because the enriched-residual objective function (31) is less sensitive to weak transitions such as boundary layers than strong transitions, the unweighted enriched residual (21) is not an appropriate objective function, despite its success for inviscid problems [54, 52, 26, 25, 39], because it will effectively ignore the boundary layer. Instead, we choose ρ in the objective function (31) to be

$$\rho : K \mapsto \begin{cases} \lambda, & K \in \mathcal{E}_{h,q}^{\text{wall}} \\ 1, & \text{otherwise,} \end{cases} \quad (42)$$

where $\lambda \geq 1$ is a boundary layer amplification factor and $\mathcal{E}_{h,q}^{\text{wall}} \subset \mathcal{E}_{h,q}$ is the subset of the elements of the mesh with at least one boundary touching a viscous wall. The impact of the boundary layer scaling on the enriched residual is demonstrated in Figure 1. Boundary layer scaling is critical in obtaining accurate solutions to shock-dominated viscous flows using implicit shock tracking, particularly with regard to prediction of heat flux profiles (Section 4.2.5).

3.5.4. Step length constraint

Non-physical states and oscillations are often a byproduct of the flow variables changing too rapidly when far from the solution. To avoid these instabilities, we employ an increment-limiting strategy that restricts the maximum step length for the line search [36, 50]. To this end, let $\phi_k^{(j)}(\cdot; \Xi) : \Omega_0 \rightarrow \mathbb{R}_{>0}$ denote a positive, scalar-valued function over domain defined from the SQP iterate $\mathbf{u}_k^{(j)}(\Xi)$ and let $\Delta\phi_k^{(j)}(\cdot; \Xi) : \Omega_0 \rightarrow \mathbb{R}_{>0}$ be its proposed modification defined from $\Delta\mathbf{z}_k^{(j)}(\Xi)$. With the goal of limiting the change in $\phi_k^{(j)}(\Xi)$, we define the function

$$\iota_k^{(j)} : (X; \Xi) \mapsto \begin{cases} 1, & d_k^{(j)}(X; \Xi) \leq \theta_l \\ 0, & d_k^{(j)}(X; \Xi) \geq \theta_u \\ \theta_l/d_k^{(j)}(X; \Xi), & d_k^{(j)}(X; \Xi) \in (\theta_l, \theta_u), \end{cases} \quad (43)$$

where $d_k^{(j)}(\cdot; \Xi) : \Omega_0 \rightarrow \mathbb{R}$ is the relative change with $d_k^{(j)} : (X; \Xi) \mapsto |\Delta\phi_k^{(j)}(X; \Xi)|/\phi_k^{(j)}(X; \Xi)$, $\theta_l \in \mathbb{R}_{>0}$ is the largest relative change that will be allowed a full Newton step (unit step length), and $\theta_u \in \mathbb{R}_{>0}$ is the smallest relative change that will be rejected (zero step length). The minimum of the pointwise function (43) over the quadrature nodes of the mesh $\mathcal{E}_{h,q}$ defines the maximum step length, i.e.,

$$\hat{\alpha}_k^{(j)}(\Xi) = \min_{X \in \Lambda_{h,q}} \iota_k^{(j)}(X; \Xi), \quad (44)$$

where $\Lambda_{h,q} \subset \Omega_0$ is the collection of quadrature nodes associated with the mesh $\mathcal{E}_{h,q}$. In this work, we apply this procedure to both the density and pressure (using whichever step length is smaller) and take $\theta_l = 0.1$ and $\theta_u = 10$. Assuming the current iterate $\mathbf{u}_k^{(j)}(\Xi)$ is free of negative densities and pressures, this procedure ensures they will not be introduced during the update from $\mathbf{z}_k^{(j)}(\Xi)$ to $\tilde{\mathbf{z}}_{k+1}^{(j)}(\Xi)$.

3.5.5. Step modification

Robustness of the SQP solver (Section 3.2) is further improved by occasionally freezing the mesh $\mathbf{x}_k^{(j)}$ and updating only the flow variables to satisfy the constraint of (29). This flexibility is afforded by the step modification function $\chi_k^{(j)}(\cdot; \Xi)$ that maps the candidate step $\tilde{\mathbf{z}}_{k+1}^{(j)}(\Xi)$ to the actual step $\mathbf{z}_{k+1}^{(j)}(\Xi)$. In practice, the constraint cannot be satisfied until the mesh optimization is complete because we do not use any artificial stabilization. Instead, we only require the magnitude of the constraint residual reduces by a preset amount. To this end, let $\tilde{\mathbf{u}}^{(j)}(\cdot, \cdot; \Xi) : \mathbb{R}^{N_u^{(j)}} \times \mathbb{R}^{N_x} \rightarrow \mathbb{R}^{N_u^{(j)}}$ be any function that satisfies

$$\left\| \mathbf{r}^{(j)}(\tilde{\mathbf{u}}^{(j)}(\mathbf{u}, \mathbf{x}; \Xi), \mathbf{x}; \Xi) \right\| < \epsilon \left\| \mathbf{r}^{(j)}(\mathbf{u}, \mathbf{x}; \Xi) \right\| \quad (45)$$

for any $\mathbf{u} \in \mathbb{R}^{N_u^{(j)}}$ and $\mathbf{x} \in \mathbb{R}^{N_x}$, where $\epsilon \in (0, 1)$ is a user-defined parameter (in this work, $\epsilon = 0.9$). Then, we define the step modification function as

$$\chi_k^{(j)} : ((\mathbf{u}, \mathbf{y}); \Xi) \mapsto \begin{cases} (\tilde{\mathbf{u}}^{(j)}(\mathbf{u}, \phi(\mathbf{y}); \Xi), \mathbf{y}), & |k/\omega_{\text{mod}}| = k/\omega_{\text{mod}} \\ (\mathbf{u}, \mathbf{y}), & \text{otherwise,} \end{cases} \quad (46)$$

where the modification is only applied every ω_{mod} iterations. We use pseudo-transient continuation (PTC) [29, 36, 50] applied to the nonlinear system $\mathbf{r}^{(j)}(\mathbf{u}, \mathbf{x}; \Xi)$ to evaluate the function $\tilde{\mathbf{u}}$. To safeguard this process, which is particularly important at early iterations before the mesh has been substantially compressed, we take n_{ptc} PTC steps (in this work, $n_{\text{ptc}} = 5$) and only accept the modification if (45) is satisfied.

3.5.6. Hessian regularization

Following the work in [26], we take the regularization matrix to be

$$\mathbf{D}_k^{(j)}(\Xi) = \partial_{\mathbf{y}} \phi(\mathbf{y}_j^{(k)}(\Xi))^T \hat{\mathbf{D}}_k^{(j)}(\Xi) \cdot \partial_{\mathbf{y}} \phi(\mathbf{y}_j^{(k)}(\Xi)), \quad (47)$$

where $\hat{\mathbf{D}}_k^{(j)}(\Xi) \in \mathbb{R}^{N_x \times N_x}$ is the stiffness matrix of a continuous Galerkin finite element discretization of the linear elasticity equations. To avoid bulging of high-order elements, we set the Poisson's ratio to $\nu = 0$. Unlike [26], which was tailored to inviscid problems, selection of the Young's modulus field is delicate for viscous problems. First, we observed that a discontinuous Young's modulus field leads to mesh degradation, which was particularly troublesome when compressing elements into thin features. Therefore, we choose the Young's modulus to lie in the piecewise linear, continuous space $E(\cdot; \Xi) \in \mathcal{W}_{h,1}$. Next, we aim to stiffen the mesh in regions where the objective function is small and allow larger deformations other regions. The enriched residual can vary by several orders of magnitude in adjacent elements, which would be poorly represented by the $\mathcal{W}_{h,1}$ space, so we first introduce $\hat{C}(\cdot; \Xi) \in \mathcal{W}_{h,1}$, where \hat{C} is the L^2 projection of the logarithm of the normalized elemental enriched residual, i.e., $C(\cdot; \Xi) : \Omega_0 \rightarrow \mathbb{R}_{\geq 0}$ with

$$C : (X, \Xi) \mapsto \log_{10} \left(\frac{\left\| (\hat{\mathbf{P}}_{K(X)}^{(j)})^T \mathbf{R}_\rho^{(j)}(\mathbf{u}_k^{(j)}(\Xi), \phi(\mathbf{y}_k^{(j)}(\Xi)); \Xi) \right\|}{\max_{K' \in \mathcal{E}_{h,q}} \left\| (\hat{\mathbf{P}}_{K'}^{(j)})^T \mathbf{R}_\rho^{(j)}(\mathbf{u}_k^{(j)}(\Xi), \phi(\mathbf{y}_k^{(j)}(\Xi)); \Xi) \right\|} \right), \quad (48)$$

where $K(X) \in \mathcal{E}_{h,q}$ is the element in which $X \in \Omega_0$ lies. The logarithm transforms a variable that varies over many orders of magnitude to one that varies over a more limited range. Finally, we define the Young's modulus field by converting back to the original scale, applying a range transformation, and converting the compliance (C) into the stiffness, we have

$$E : (X; \Xi) \mapsto g(10^{\hat{C}(X; \Xi)}; \Xi)^{-1}, \quad (49)$$

where $g(\cdot; \Xi) : [0, 10^{\hat{C}_{\max}(\Xi)}] \rightarrow [C_1, C_u]$ with $g : (s; \Xi) \mapsto C_u \theta(s; \Xi) + C_1(1 - \theta(s; \Xi))$ is the range transformation, $\theta(\cdot; \Xi) : [0, 10^{\hat{C}_{\max}(\Xi)}] \rightarrow [0, 1]$ is a smooth cutoff function

$$\theta : (s; \Xi) \mapsto \frac{1}{2} \left(\sin \left(\pi \frac{s}{10^{\hat{C}_{\max}(\Xi)}} - \frac{\pi}{2} \right) + 1 \right), \quad (50)$$

(C_1, C_u) is the range of g ($C_1 = 1$ and $C_u = 10$ in this work), and $\hat{C}_{\max}(\Xi) = \sup_{X \in \Omega_0} \hat{C}(X; \Xi)$. A comparison between the Young's modulus distribution in [54] and the proposed enriched residual-based distribution is illustrated in Figure 2.

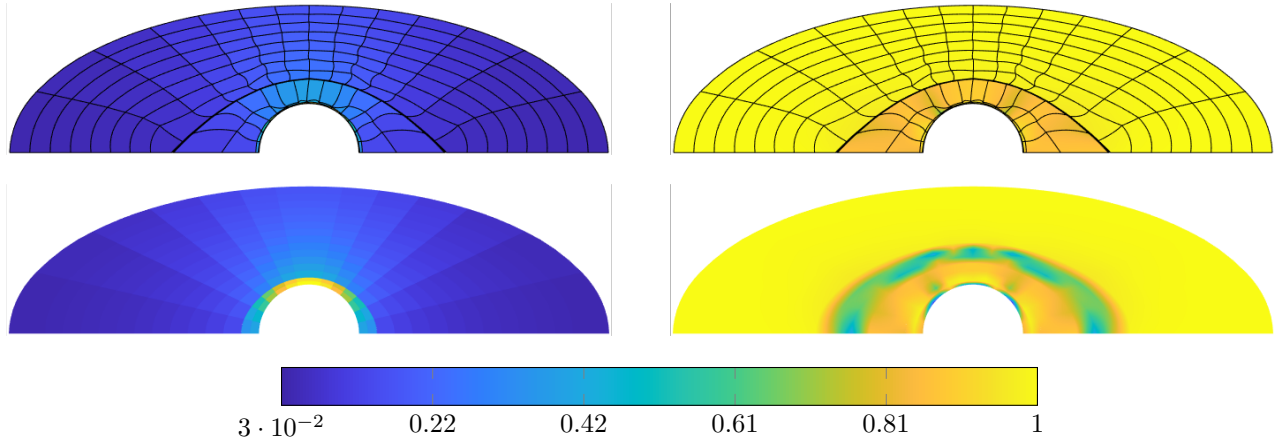


Figure 2: Distribution of the Young's modulus field E based on the inverse volume of reference mesh [54] (left) and the enriched residual (right) for $M_\infty = 5$, $\text{Re} = 10^3$ hypersonic flow over a cylinder (prior to p -adaptation). The Young's modulus are provided on the physical domain (top) and reference domain (bottom) for clarity.

The regularization matrix $\mathbf{D}_k^{(j)}(\Xi)$ controls the behavior of the regularization across the domain Ω_0 . On the other hand, the regularization parameter $\gamma_k^{(j)}(\Xi)$ controls the magnitude of the regularization, which must be carefully balanced. Too little regularization leads to aggressive steps and poor mesh quality, whereas too much regularization leads to minuscule step sizes. Furthermore, it is important to have more regularization at early iterations when the mesh and solution are far from convergence. To this end, we define the regularization parameter as

$$\gamma_k^{(j)}(\Xi) = \frac{\hat{\gamma}}{\Xi^{\eta_1} k^{\eta_2}}, \quad (51)$$

where $\hat{\gamma}, \eta_1, \eta_2 \in \mathbb{R}_{\geq 0}$ are user-defined parameters ($\eta_1 > 0$ if $\{\Xi_1, \dots, \Xi_c\}$ is an increasing sequence, e.g., Ξ represents Reynolds number, and $\eta_2 < 0$ if $\{\Xi_1, \dots, \Xi_c\}$ is a decreasing sequence, e.g., Ξ represents viscosity). The explicit dependence on the optimization iteration k and continuation parameter Ξ drives the regularization parameter toward zero as the SQP and continuation iterations progress.

Remark 4. For domains with planar boundaries, the parametrization ϕ is affine in \mathbf{y} , which means its derivative is independent of \mathbf{y} . In these cases, $\mathbf{D}_k^{(j)}(\Xi)$ does not depend on the state $\mathbf{y}_k^{(j)}(\Xi)$.

3.5.7. Viscosity continuation

In the context of implicit shock tracking, continuation has been used to solve high-speed, inviscid flows by using continuation with respect to Mach number [25]. For viscous flows, continuation with respect to viscosity is necessary to avoid carbuncles and compress the mesh into thin shock and boundary layers. By starting with a large viscosity, these features are thicker, which can easily be detected on coarse, shock-agnostic meshes and require less extreme mesh compression to adequately resolve. Once a reasonable mesh is obtained for the large, initial viscosity (Ξ_0), the viscosity is decreased (to Ξ_1) and the previous solution (mesh and flow variables) are used to initialize the SQP solver. This process is repeated until the target viscosity is obtained (Ξ_*). Viscosity-based continuation was first introduced in the context of implicit shock tracking in [31], and we demonstrate its importance in avoiding carbuncles in Section 4.2.3. Finally, we found that, provided continuation is sufficiently gradual to avoid carbuncles, the final solution is relatively insensitive to the continuation strategy.

Remark 5. *As is always the case with continuation, it is unnecessary to deeply converge the optimization problems for intermediate viscosities, i.e., $\Xi \neq \Xi_*$. In practice, a predefined number of SQP iterations are performed for all intermediate viscosities.*

3.6. Summary

To close this section, the complete HOIST method for viscous conservation laws is summarized in Algorithms 1-3. Algorithm 1 summarizes the HOIST method for a fixed continuation parameter and p -adaptation level to define the HOIST function (r -adaptation only). Algorithm 2 incorporates continuation into HOIST to define HOISTC for a fixed p -adaptation level (r -adaptation only). Finally, Algorithm 3 summarizes the complete p -adaptive HOIST method with continuation (rp -adaptation).

Algorithm 1 HOIST method for viscous problems (HOIST)

Input: Continuation parameter Ξ , p -adaptivity iteration j , initial state $\mathbf{u}_0^{(j)}(\Xi)$ and mesh $\mathbf{y}_0^{(j)}(\Xi)$, user-defined parameters $(\Delta, \kappa, \theta_1, \theta_u, \epsilon, \omega_{\text{mod}}, C_1, C_u, \hat{\gamma}, \eta_1, \eta_2)$

Output: Converged state $\mathbf{u}_*^{(j)}(\Xi)$ and mesh $\mathbf{y}_*^{(j)}(\Xi)$

- 1: **Residual scaling:** Compute ρ from (42) to emphasize boundary layers
 - 2: **for** $k = 1, 2, \dots$ **do**
 - 3: **Convergence check:** Terminate iterations if first-order optimality conditions of (29) are satisfied [54, 26]
 - 4: **SQP search direction:** Compute $\Delta \mathbf{z}_k^{(j)}(\Xi)$ from (35) with regularization matrix from (47)–(51)
 - 5: **Step length constraint:** Compute $\hat{\alpha}_k^{(j)}(\Xi)$ from (44)
 - 6: **Line search:** Compute step size $\alpha_k^{(j)}(\Xi) \in (0, \hat{\alpha}_k^{(j)}(\Xi)]$ such that ℓ_1 merit function [26] satisfies sufficient decrease condition [40]
 - 7: **SQP update:** Compute $\tilde{\mathbf{z}}_{k+1}^{(j)}(\Xi)$ from (34)
 - 8: **State modification:** Compute $\mathbf{z}_{k+1}^{(j)}(\Xi)$ from (34) with $\chi_k^{(j)}$ defined in (46)
 - 9: **end for**
 - 10: **Finalize solution:** $\mathbf{u}_*^{(j)}(\Xi) \leftarrow \mathbf{u}_k^{(j)}(\Xi)$ and $\mathbf{y}_*^{(j)}(\Xi) \leftarrow \mathbf{y}_k^{(j)}(\Xi)$
-

Algorithm 2 HOIST method for viscous problems with continuation (HOISTC)

Input: Continuation sequence $\{\Xi_1, \dots, \Xi_c = \Xi_*\}$, p -adaptivity iteration j , initial state $\mathbf{u}_0^{(j)}(\Xi_1)$ and mesh $\mathbf{y}_0^{(j)}(\Xi_1)$, user-defined parameters $\Upsilon := (\Delta, \kappa, \theta_1, \theta_u, \epsilon, \omega_{\text{mod}}, C_1, C_u, \hat{\gamma}, \eta_1, \eta_2)$

Output: Converged state $\mathbf{u}_*^{(j)}(\Xi_*)$ and mesh $\mathbf{y}_*^{(j)}(\Xi_*)$

- 1: **for** $i = 1, \dots, c$ **do**
 - 2: **IST solve:** $(\mathbf{u}_*^{(j)}(\Xi_i), \mathbf{y}_*^{(j)}(\Xi_i)) = \text{HOIST}(\Xi_i, j, \mathbf{u}_0^{(j)}(\Xi_i), \mathbf{y}_0^{(j)}(\Xi_i), \Upsilon)$
 - 3: **Continuation update:** $\mathbf{u}_0^{(j)}(\Xi_{i+1}) = \mathbf{u}_*^{(j)}(\Xi_i)$ and $\mathbf{y}_0^{(j)}(\Xi_{i+1}) = \mathbf{y}_*^{(j)}(\Xi_i)$
 - 4: **end for**
-

Algorithm 3 HOIST method for viscous problems with continuation and p -adaptivity (pHOISTC)

Input: Continuation sequence $\{\Xi_1, \dots, \Xi_c = \Xi_\star\}$, initial state $\mathbf{u}_0^{(0)}(\Xi_1)$ and mesh $\mathbf{y}_0^{(0)}(\Xi_1)$, user-defined parameters $\Upsilon := (\Delta, \kappa, \theta_1, \theta_u, \epsilon, \omega_{\text{mod}}, C_1, C_u, \hat{\gamma}, \eta_1, \eta_2)$, p -adaptivity convergence parameters $\hat{\epsilon}$ and J_{max}

Output: Converged state $\mathbf{u}_\star^{(J)}(\Xi_\star)$ and mesh $\mathbf{y}_\star^{(J)}(\Xi_\star)$

- 1: **IST continuation:** $(\mathbf{u}_\star^{(0)}(\Xi_\star), \mathbf{y}_\star^{(0)}(\Xi_\star)) = \text{HOISTC}(\{\Xi_1, \dots, \Xi_c\}, 0, \mathbf{u}_0^{(0)}(\Xi_1), \mathbf{y}_0^{(0)}(\Xi_1), \Upsilon)$
 - 2: **for** $j = 1, \dots, J_{\text{max}}$ **do**
 - 3: **Convergence check:** Terminate iterations if conditions in (41) satisfied with $J = j$
 - 4: **IST solve:** $(\mathbf{u}_\star^{(j)}(\Xi_\star), \mathbf{y}_\star^{(j)}(\Xi_\star)) = \text{HOIST}(\Xi_\star, j, \mathbf{u}_\star^{(j-1)}(\Xi_\star), \mathbf{y}_\star^{(j-1)}(\Xi_\star), \Upsilon)$
 - 5: **end for**
-

4. Numerical experiments

In this section, we apply the proposed rp -adaptive HOIST method to three viscous Burgers' equation examples (Section 4.1) and two steady Navier-Stokes examples (Section 4.2) to demonstrate its ability to accurately resolve viscous shocks (both straight-sided and curved) and boundary layers, and accurately predict quantities of interest (both integrated and profiles). We use the most interesting example, hypersonic flow over a cylinder (Section 4.2.2), to demonstrate the importance of the various solver enhancements proposed in this work.

4.1. Viscous Burgers' equation

The time-dependent, viscous Burgers' equation governs nonlinear advection of a scalar quantity $\phi : \Omega \rightarrow \mathbb{R}$ through a one-dimensional domain $\Omega \subset \mathbb{R}$

$$\frac{\partial}{\partial t} \phi(x, t) + \phi(x, t) \frac{\partial}{\partial x} \phi(x, t) = \nu \frac{\partial^2}{\partial x^2} \phi(x, t) \quad (52)$$

for all $x \in \Omega$ and $t \in \mathcal{T}$ with diffusion coefficient $\nu \in \mathbb{R}_{\geq 0}$. This unsteady problem is written as a conservation law of the form (1) using a space-time formulation [31, 53].

4.1.1. Straight-sided space-time shock: pure r -adaptivity

First, we consider the example from [31], where $\Omega = (0, 1)$ and $\mathcal{T} = (0, 1)$ with initial condition $\phi(x, 0) = \sin(2\pi x)/\pi + 0.2$ and constant boundary conditions that are consistent with the initial condition. The sine wave steepens into a viscous shock with thickness proportional to the viscosity, which then propagates. We use this simple problem to demonstrate the capability of the viscous HOIST method to resolve thin shocks with pure r -adaptation (no p -adaptation).

We discretize the space-time domain using a structured mesh of 384 straight-sided ($q = 1$) triangles with quadratic solution approximation ($p : K \mapsto 2$). The HOIST solver is initialized from a first-order finite volume solution of (52) with $\nu = 10^{-3}$ on the structured mesh (Figure 3). Viscosity continuation is performed in 11 stages with $\Xi_i = (1 - 9(i - 1)/100) \cdot 10^{-3}$ for $i = 1, 2, \dots, 11$ with each continuation stage allotted 100 SQP iterations. For this problem, we do not use residual weighting (Section 3.5.3), step length modifications (Section 3.5.4) or step modifications (Section 3.5.5) as they proved unnecessary, and we used the Hessian regularization matrix of [54]. The enrichment degree is $\Delta = 2$. Due to the low polynomial degree used ($p : K \mapsto 2$), three layers of elements are compressed into the shock thickness, which decreases with viscosity as $\mathcal{O}(\nu)$, to accurately resolve the steep gradient. At the final viscosity $\nu = 10^{-4}$, the shock is extremely thin. The HOIST method also compresses the mesh near the evolving peaks of the sine wave (gradient changes sign) and near the shock formation singularity (Figure 4). In the reference domain Ω_0 , where the mesh is decompressed, the internal shock structure can be clearly seen (Figure 5). Both of these figures demonstrate that the space-time solution is well-resolved by the r -adaptation approach. Temporal slices of the spatial solution field further show the solution is well-resolved and oscillation-free, and the viscous shock is represented as a continuous feature (Figure 6). Furthermore, temporal slices of the HOIST solution match a reference solution computed with a second-order finite volume method with superbee limiter on a grid with 2000 cells that is integrated with fourth-order Runge-Kutta (explicit) with fixed time step $\Delta t = 0.0005$.

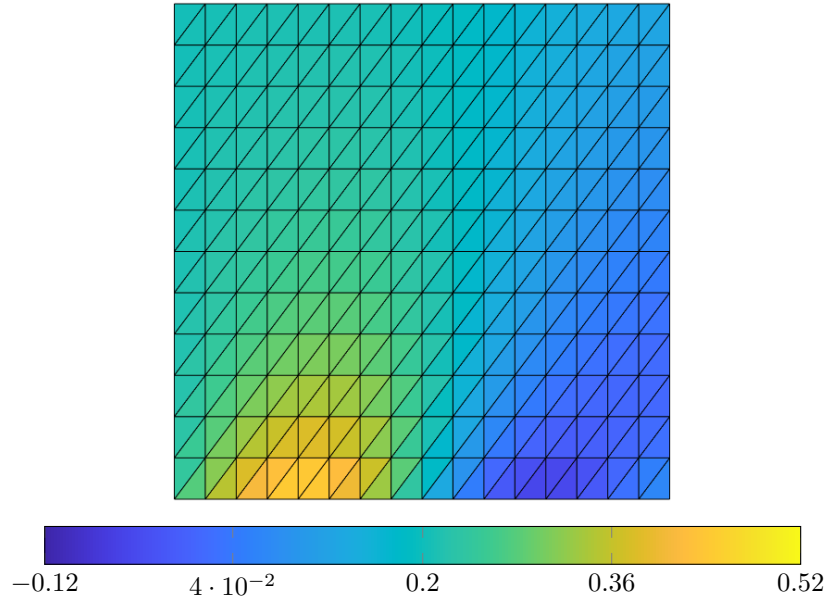


Figure 3: Mesh and solution (first-order finite volume with $\nu = 10^{-3}$) used to initialize HOIST method (pure r -adaptation) for viscous Burgers' problem with straight shock.

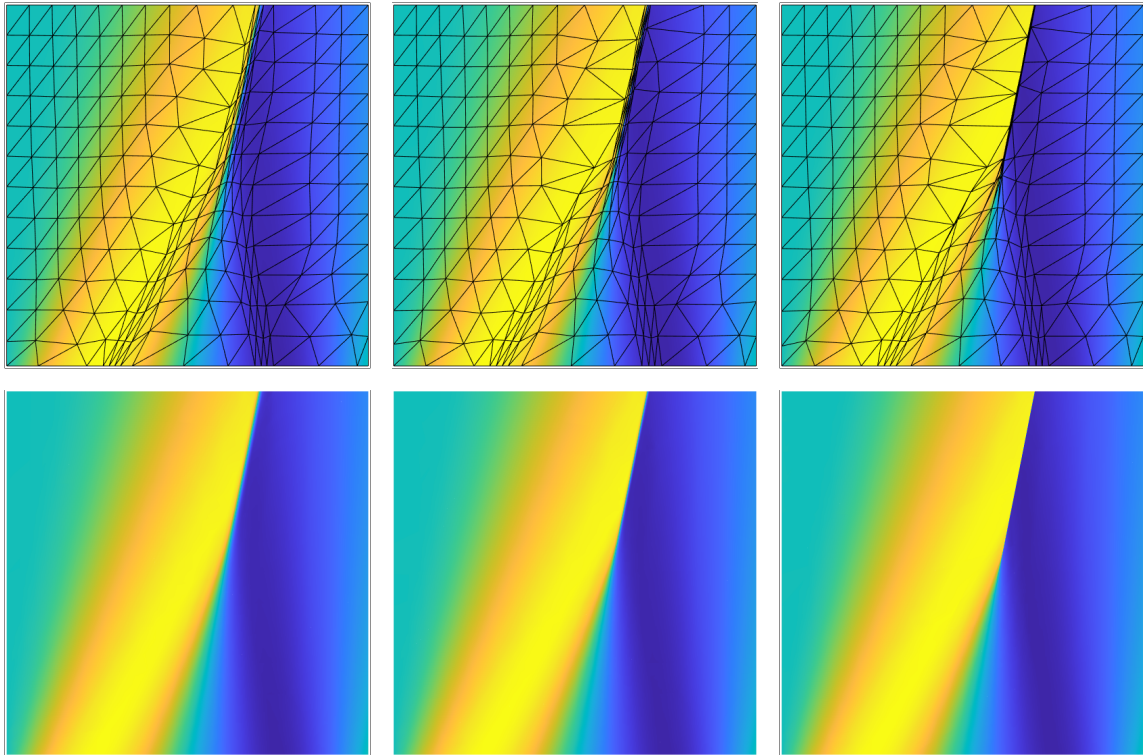


Figure 4: HOIST solution (pure r -adaptation) in the physical domain $\mathcal{G}(\Omega_0)$ to the viscous Burgers' problem with straight shock at $\nu = 10^{-3}, 5 \times 10^{-4}, 10^{-4}$ (left-to-right) with and without mesh edges shown. Colorbar in Figure 3.

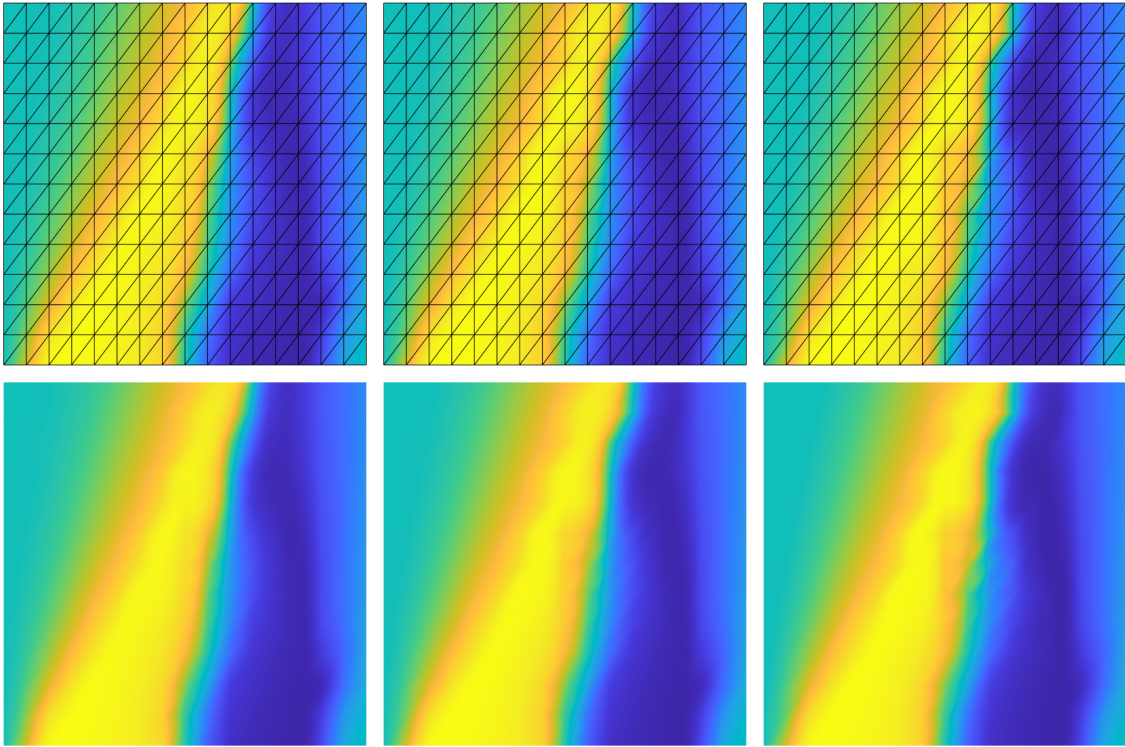


Figure 5: HOIST solution (pure r -adaptation) in the reference domain Ω_0 to the viscous Burgers' problem with straight shock at $\nu = 10^{-3}, 5 \times 10^{-4}, 10^{-4}$ (left-to-right) with and without mesh edges shown. Colorbar in Figure 3.

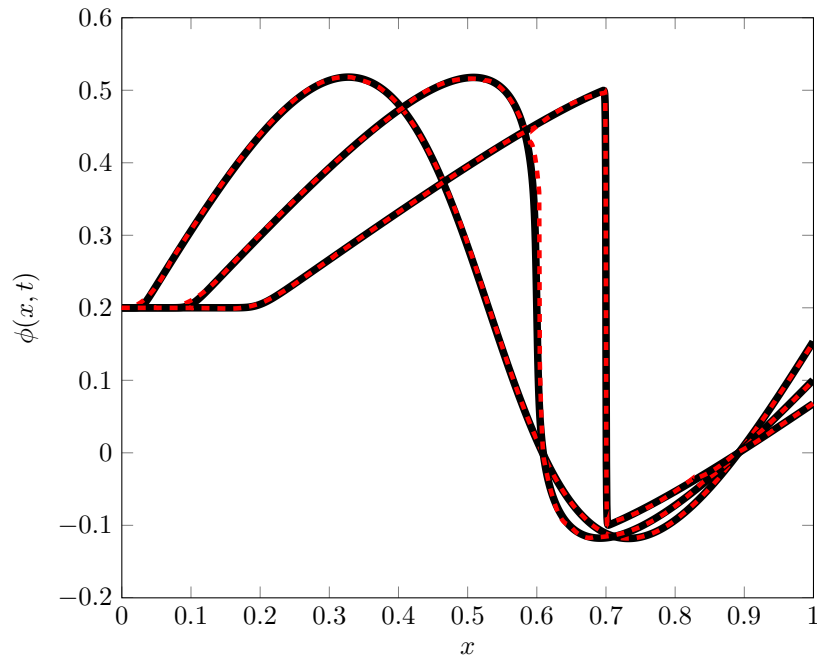


Figure 6: Temporal slices of the HOIST solution (pure r -adaptation) at times $t \in \{0.15, 0.5, 1.0\}$ (---) and a reference solution computed with a highly refined second-order finite volume solution (—) for the viscous Burgers' problem with straight shock.

4.1.2. One-dimensional steady shock: r - vs. p -adaptation study

Having demonstrated the ability of the proposed HOIST method (r -adaptation only) to resolve thin viscous shocks in Section 4.1.1, we study how to balance the two refinement mechanisms considered in this work: r - and p -refinement. For this, we consider the steady viscous Burgers' equation in (52) with $\partial_t \phi = 0$ over the domain $\Omega = (-1, 1)$ with the following analytical solution

$$\phi(x) = \phi_R + \frac{\phi_L - \phi_R}{1 + \exp(x/\nu)}, \quad (53)$$

where $\phi_L = 1$ and $\phi_R = -1$ are the left and right states, respectively, of the viscous shock. To study the trade-off between r - and p -adaptation, we consider five families of polynomial degree distributions parametrized by $\hat{p} \in \mathbb{N}$ and apply the HOIST method in pure r -adaptation mode. We repeat this study for $\hat{p} = 1, 2, \dots, 9$ and $\nu = 0.1, 0.01$. This study will provide insight into the optimal distribution of the elements sizes for a given polynomial distribution and shock thickness, which help us predict the behavior of the full rp -adaptive HOIST method. Because this problem is one-dimensional and relatively simple, none of the robustness measures in Section 3.5 were used, except the enrichment degree $\Delta = 2$.

The first family considers a mesh with a single element with polynomial degree $\hat{p}_1 : K \mapsto \hat{p}$. This corresponds to a global polynomial approximation, which is expected to poorly approximate the viscous shock in (53), especially because there are no free nodes to move for the r -adaptation procedure; however, it is included as a control. The second family considers a mesh with three elements with polynomial degree distribution

$$\hat{p}_2 : K \mapsto \begin{cases} \hat{p}, & K = (-1/3, 1/3) \\ 1, & \text{otherwise.} \end{cases} \quad (54)$$

The remaining families consider a mesh with five elements with polynomial degree distributions

$$\begin{aligned} \hat{p}_3 : K &\mapsto \begin{cases} \hat{p}, & K \in \{(-0.6, -0.2), (0.2, 0.6)\} \\ 1, & \text{otherwise} \end{cases} \\ \hat{p}_4 : K &\mapsto \begin{cases} \hat{p}, & K \in \{(-0.6, -0.2), (0.2, 0.6)\} \\ 3, & K = (-0.2, 0.2) \\ 1, & \text{otherwise} \end{cases} \\ \hat{p}_5 : K &\mapsto \begin{cases} \hat{p}, & K \in \{(-0.6, -0.2), (0.2, 0.6)\} \\ 5, & K = (-0.2, 0.2) \\ 1, & \text{otherwise.} \end{cases} \end{aligned} \quad (55)$$

The different polynomial distributions lead to very different optimized meshes (Figure 7). For family \hat{p}_2 , the central element is contained within the shock thickness for lower degrees ($\hat{p} \leq 4$ for $\nu = 0.1$ and $\hat{p} \leq 6$ for $\nu = 0.01$), and expands somewhat beyond for higher degrees. The extent to which the central element expands beyond the shock thickness depends on both approximation degree and viscosity; for $\nu = 0.01$, expansion beyond the shock thickness is limited even for $\hat{p} = 9$. For the \hat{p}_3 family, which forces the central element to use a linear approximation, the optimal element sizes grow as \hat{p} increases. However, because the central element uses a linear approximation, it is forced to be very small, especially for larger values of \hat{p} , because the linear approximation is only valid in the neighborhood of $x = 0$. The elements adjacent to the central element can be much larger than the shock element in the \hat{p}_2 family because each one is only approximating half of the transition. Owing to their similarity, \hat{p}_4 and \hat{p}_5 families show similar trends as the \hat{p}_3 family. The main difference comes from the smallness requirement on the central element. While the central element is forced to be minuscule for the \hat{p}_3 family, especially for $\nu = 0.01$, it can be much larger in the \hat{p}_4 and \hat{p}_5 families because of its cubic and quintic approximation, respectively; however, it still remains within the shock. For low values of \hat{p} , the central element is nearly the entire shock width because the cubic/quintic approximation is needed to resolve the shock transition and low-order approximations are forced to the regions where the solution is nearly constant. Finally, we observe that the low-order ($\hat{p} = 1, 2$) members of the \hat{p}_2 , \hat{p}_3 , and \hat{p}_4 families have three elements compressed in the shock thickness for $\nu = 0.01$, which is consistent with the optimized mesh computed in Section 4.1.1. However, a quintic approximation

in the central element (\hat{p}_5 family) relaxes this requirement by allowing the other elements to extend beyond the shock thickness. This behavior is also produced by enriching the approximation degree of the elements adjacent to the central element (\hat{p}_3 and \hat{p}_4 families).

Despite the substantially different meshes produced for the different polynomial degree distributions, the $L^2(\Omega_0)$ for all families decays at roughly the same rate with respect to the number of flow variable degrees of freedom (N_u) (Figure 8), and have similar error constants. The one exception is the global polynomial degree \hat{p}_1 , which, as expected, only decays for the larger viscosity where the shock is a relatively slow transition. From this study, we conclude that there is not a preferred approach to balance r - and p -adaptation, at least in terms of error vs the number of degrees of freedom. However, the optimal mesh strongly depends on the chosen polynomial distribution. This means that the balance between r - and p -adaptation can be chosen based on other criteria, e.g., realizability of the optimal mesh, computational cost, or overall convenience. In the rp -adaptation setting, we expect two extremes. If r -adaptivity is prioritized at lower polynomial degrees, more element compression is expected near the shocks and boundary layers and, if the elements are sufficiently small, p -adaptation will not necessarily be focused within the shock or boundary layer. This situation would produce distributions similar to the \hat{p}_3 family. On the other hand, if p -adaptivity is prioritized, the polynomial degree in the shock and boundary layer would be rapidly increased due to underresolution, and the element compression would be more modest when r -adaptation begins, especially for larger viscosities. This situation would produce distributions similar to the \hat{p}_2 family. As we will see, the proposed rp -adaptive method tends to produce \hat{p}_3 family solutions because (1) it allows a majority of the work to be performed on the lower p discretizations with fewer degrees of freedom and (2) the element relaxation afforded by larger polynomial degrees is less beneficial for very thin features.

4.1.3. Curved space-time shock: rp -adaptivity

Next, we consider a modification of a problem found in [35], defined by the spatial domain $\Omega = (-0.4, 1)$, temporal domain $\mathcal{T} = (0, 0.8)$, and smooth initial condition

$$\phi(x, 0) = \begin{cases} \phi_L \left(-1 + \frac{2}{1 + \exp(5x)} \right) & \text{if } x \leq 0 \\ \phi_R(1 - x) \left(-1 + \frac{2}{1 + \exp(5x)} \right) & \text{if } x > 0 \end{cases} \quad (56)$$

where $\phi_L = 4$ and $\phi_R = 3$. The boundary conditions are constant in time and consistent with the initial condition. This problem features a smooth initial condition that steepens into a shock at a finite time, which then accelerates until it leaves the domain. Despite the overall simplicity of this problem, the solution possess two challenging features in the space-time domain: (1) a singularity from the shock formation and (2) a curved shock from the acceleration. We use this problem to demonstrate the full rp -adaptive HOIST method.

We initially discretize the space-time domain using a structured mesh of 100 straight-sided ($q = 1$) elements with linear solution approximation ($p_0 : K \mapsto 1$). The HOIST solver is initialized from a first-order finite volume solution of (52) with $\nu = 10^{-1}$ (Figure 9). Viscosity continuation is performed in 20 stages of equal increments beginning with $\Xi_1 = 10^{-1}$ and ending with $\Xi_{20} = 10^{-3}$ with each continuation stage allotted 10 SQP iterations. For this problem, we do not use residual weighting (Section 3.5.3), step length modifications (Section 3.5.4) or step modifications (Section 3.5.5) as they proved unnecessary, and we used the Hessian regularization matrix of [54]. The enrichment degree is $\Delta = 2$. After viscosity continuation is complete, the mesh approximation is increased to $q = 2$ and additional SQP iterations are performed for improved representation of the curved shock. A quadratic mesh could have been used from the outset; however, we found that the robustness of the SQP solver is improved and the mesh compression is more severe by initializing with $q = 1$. Finally, we perform three rounds of p -refinement using the enriched residual error indicator \hat{s}_j^{UWR} .

Prior to p -adaptation, two elements are compressed into the shock thickness and the enriched residual effectively identifies the elements inside and near the shock as the main contributors to the error. The p -refinement approach locally increases the polynomial degree in these elements and the HOIST method adjusts the mesh appropriately. In the end, the mesh has been effectively compressed near the singularity and shock, and the polynomial degrees appropriately enhanced to reduce the magnitude of the error indicator

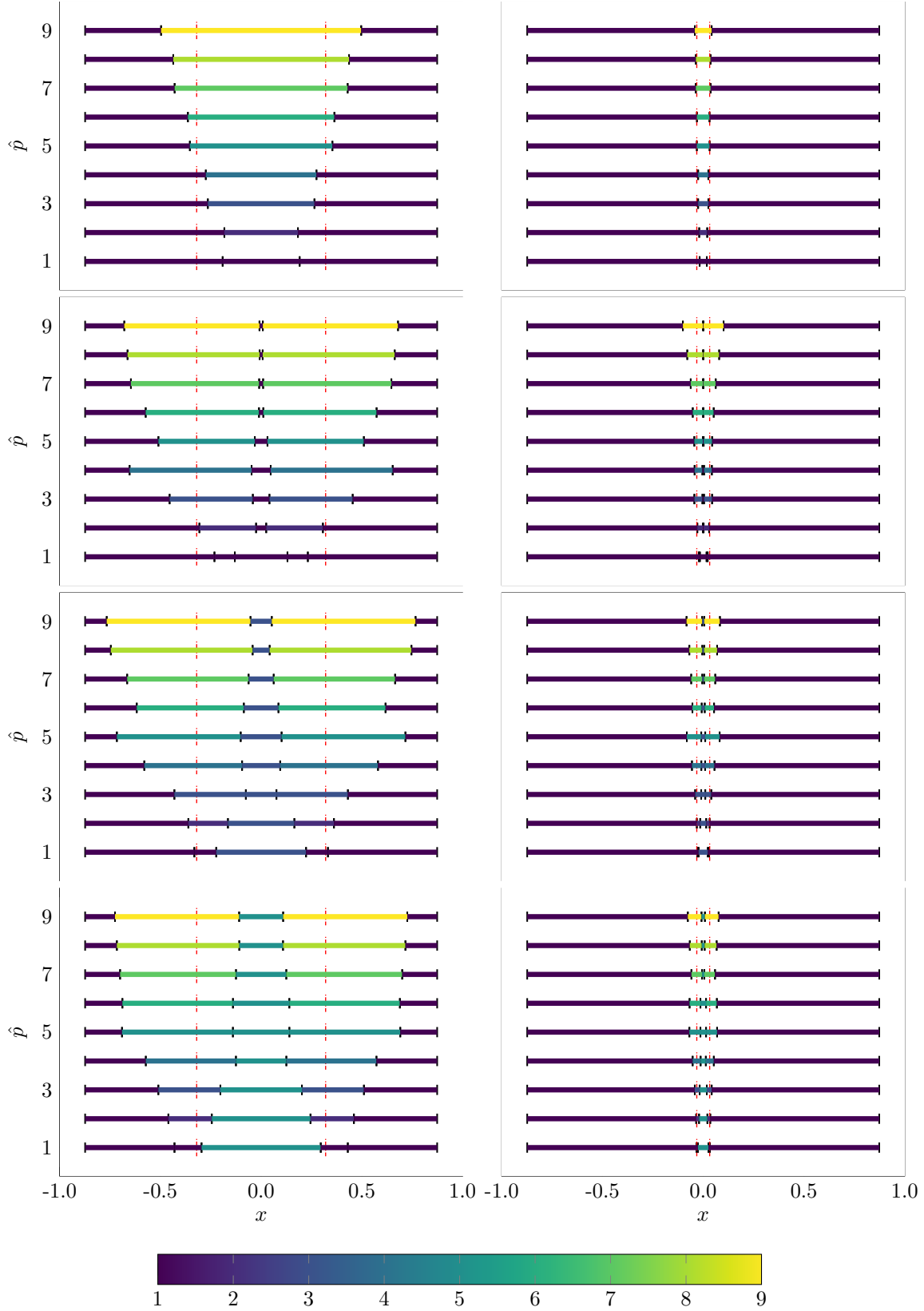


Figure 7: HOIST solution (pure r -adaptation) for the steady Burgers' problem for four families of polynomial distributions $\hat{p}_2, \hat{p}_3, \hat{p}_4, \hat{p}_5$ (top-to-bottom) for parameter $\hat{p} = 1, 2, \dots, 9$ and viscosities $\nu = 0.1$ (left) and $\nu = 0.01$ (right). The vertical lines delineate the shock thickness, defined as $x \in [-\delta, \delta]$, where $|\phi(x)| \leq 0.95 \max\{|\phi_L|, |\phi_R|\}$. The color corresponds to the polynomial degree used for each element.

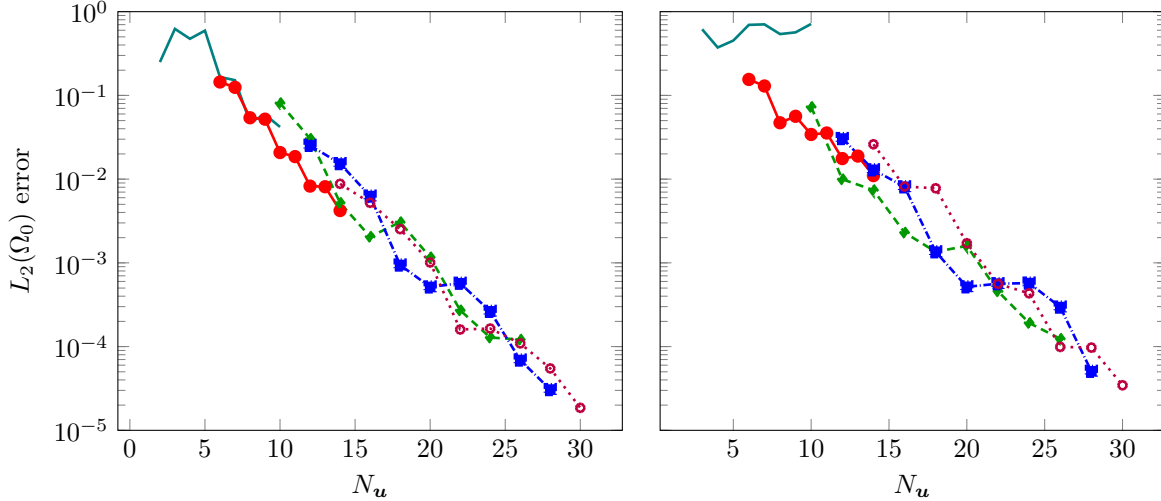


Figure 8: HOIST error (pure r -adaptation) for the steady Burgers' problem for the five families of polynomial distributions \hat{p}_1 (—), \hat{p}_2 (—●—), \hat{p}_3 (—▲—), \hat{p}_4 (—■—), \hat{p}_5 (—○—) and viscosities $\nu = 0.1$ (left) and $\nu = 0.01$ (right) as a function of the number of solution degrees of freedom.

(Figure 10). The space-time solutions in the reference domain Ω_0 clearly show the internal structure of the shock and the distribution of the polynomial degree (Figure 11). Both of these figures demonstrate that the space-time solution is well-resolved by the rp -adaptation approach. Temporal slices of the spatial solution field further show the solution is well-resolved and oscillation-free, and the viscous shock is represented as a continuous feature (Figure 12). Furthermore, temporal slices of the HOIST solution match a reference solution computed with a second-order finite volume method with superbee limiter on a grid with 2000 cells that is integrated with fourth-order Runge–Kutta (explicit) with fixed time step $\Delta t = 0.001$.

The behavior of the SQP solver across all continuation and p -adaptation stages is shown in Figure 13. For a given value of the viscosity Ξ_i and polynomial distribution p_j , the HOIST method drives the residual toward zero. However, the residual jumps up after the continuation parameter or polynomial distribution is updated because the residual function changes. Notice that 250 iterations are performed on the coarsest (i.e., least expensive) discretization that uses a linear approximations in all elements. The p -adaptation process is complete in another 150 iterations, at which point the mesh is effectively frozen. We allow the SQP solver to run an additional 300 iterations to obtain deep convergence, although a nonlinear solve on a fixed mesh could have been used to obtain the solution in only a few iterations.

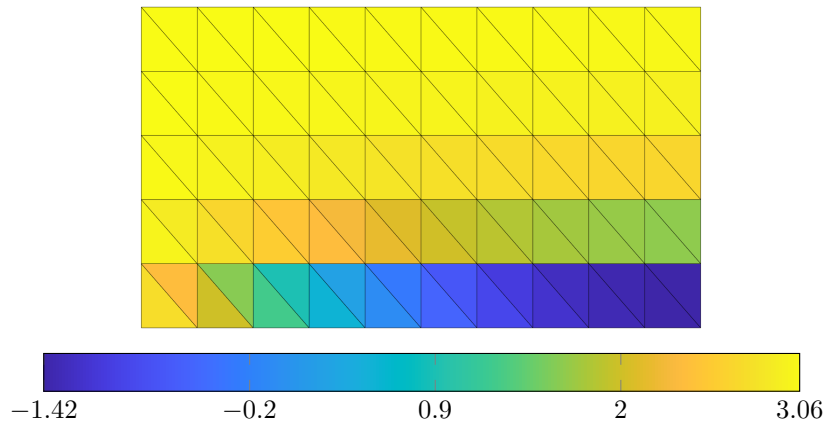


Figure 9: Mesh and solution (first-order finite volume with $\nu = 10^{-1}$) used to initialize the rp -adaptive HOIST method for the viscous Burgers' problem with curved shock.

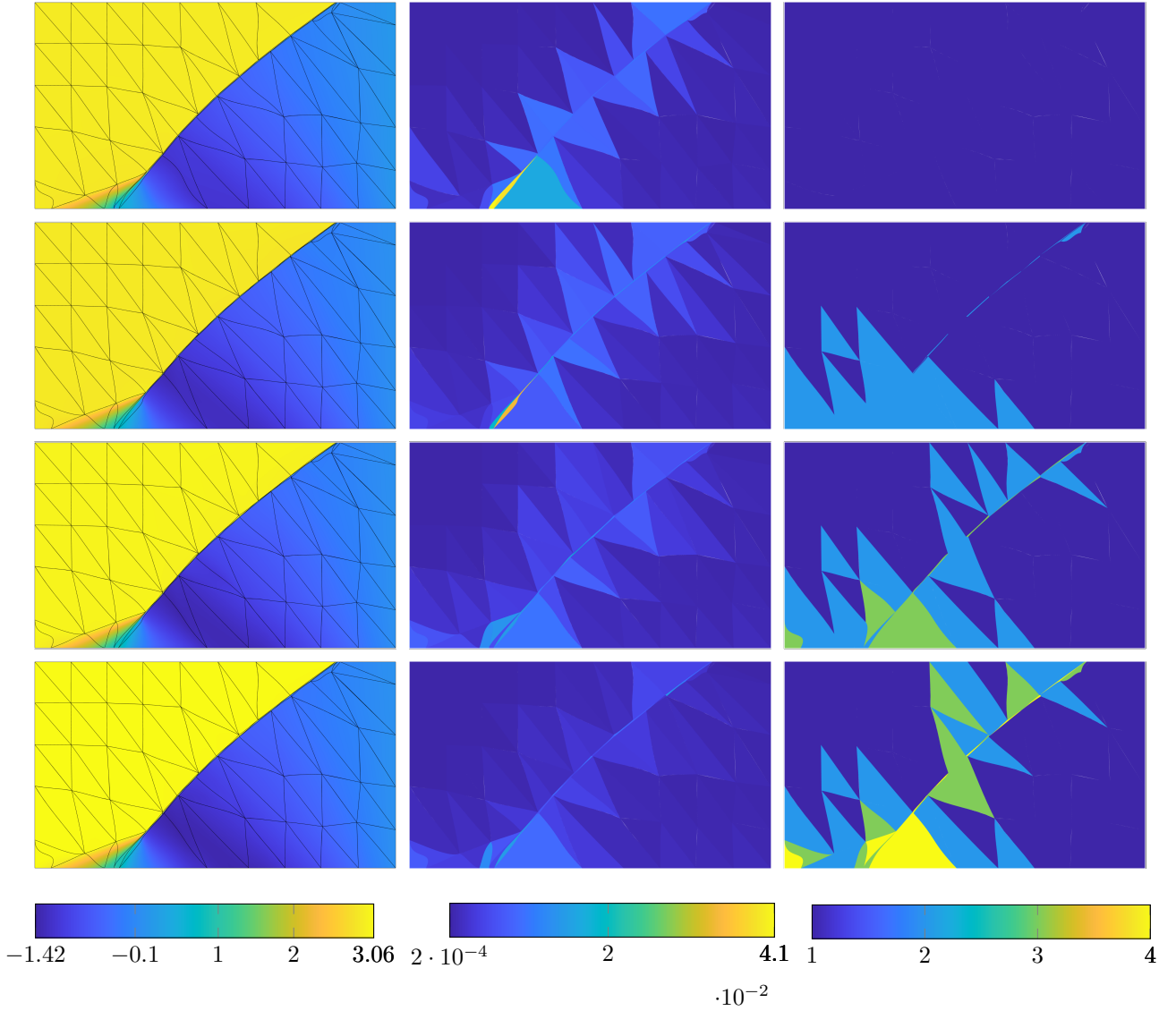


Figure 10: HOIST solution (*rp*-adaptation) (*left*), the enriched residual error indicator (*middle*), and polynomial degree distribution (*right*) in the physical domain $\mathcal{G}(\Omega_0)$ to the viscous Burgers' problem with curved shock. These quantities are provided prior to *p*-adaptation and after each *p*-adaptation iteration (*top-to-bottom*).

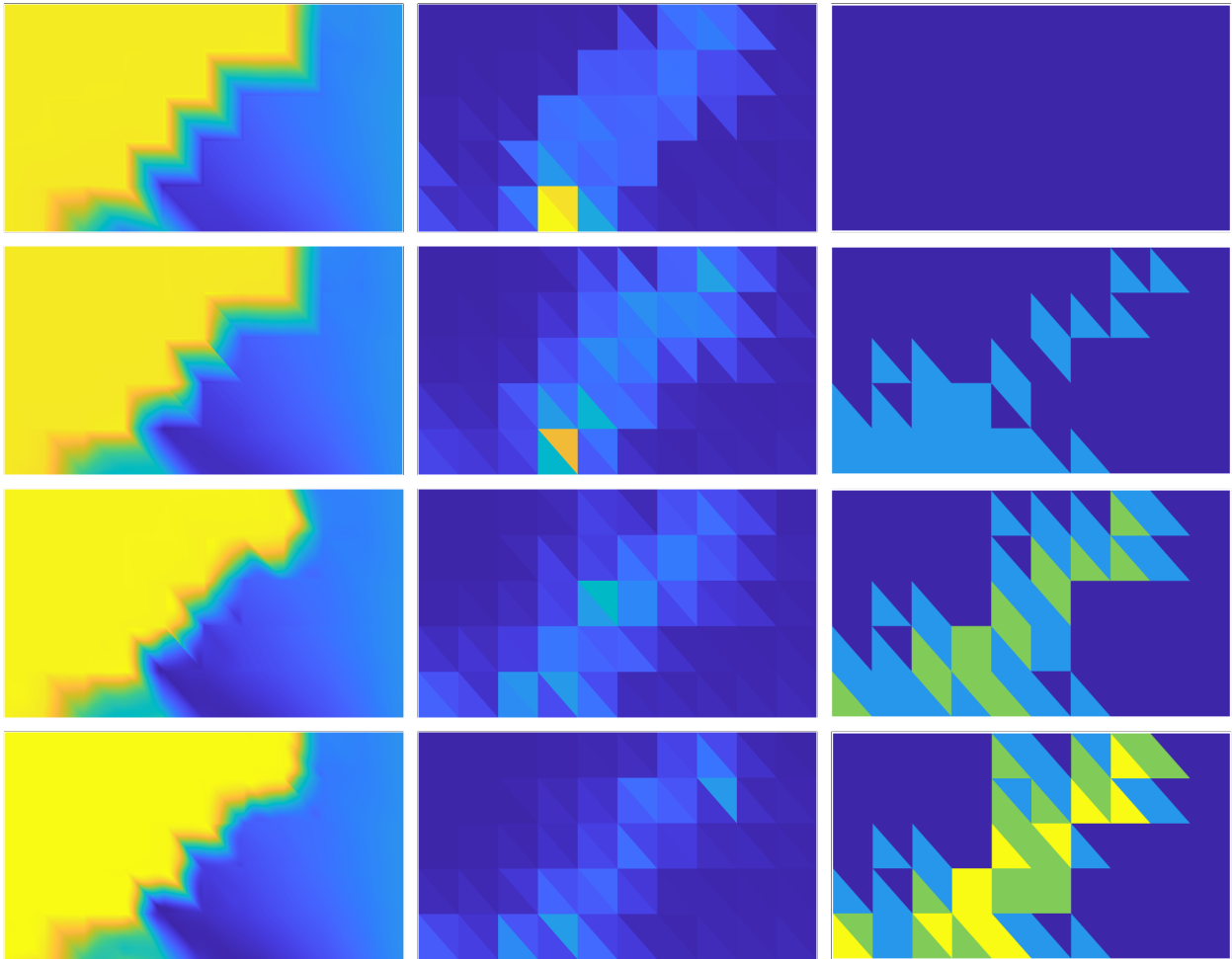


Figure 11: HOIST solution (rp -adaptation) (*left*), the enriched residual error indicator (*middle*), and polynomial degree distribution (*right*) in the reference domain to the viscous Burgers' problem with curved shock. These quantities are provided prior to p -adaptation and after each p -adaptation iteration (*top-to-bottom*). Colorbar in Figure 10.

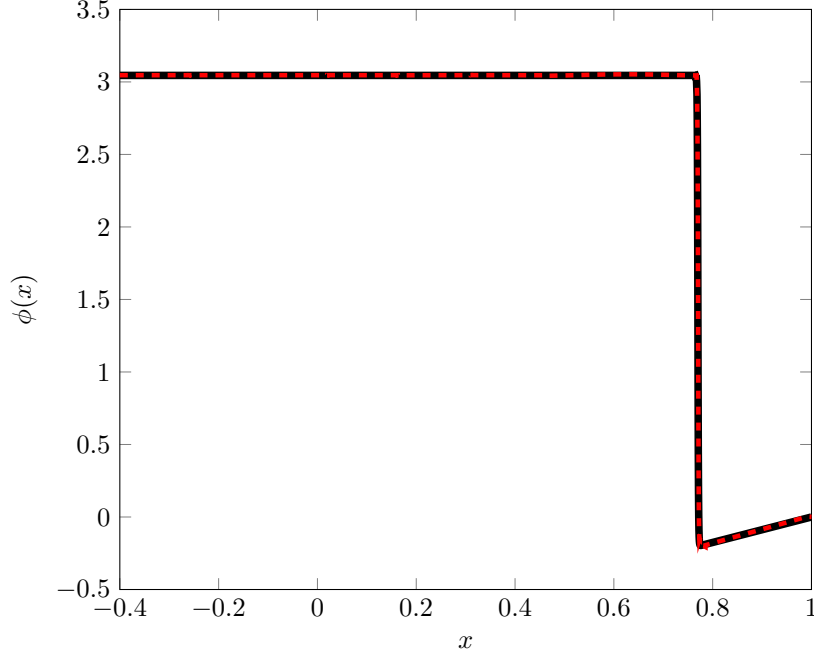


Figure 12: Temporal slice of the HOIST solution (*rp*-adaptation) at $t = 0.8$ (---) and a reference solution computed with a highly refined second-order finite volume method (—) for the viscous Burgers' problem with curved shock.

4.2. Navier-Stokes equations

Next, we consider steady compressible, viscous flow through a domain $\Omega \subset \mathbb{R}^d$ with governing equations given by

$$\begin{aligned} \frac{\partial}{\partial x_j} (\rho v_j) &= 0 \\ \frac{\partial}{\partial x_j} (\rho v_i v_j + P \delta_{ij}) &= \frac{\partial}{\partial x_j} \varpi_{ij} \\ \frac{\partial}{\partial x_j} ((\rho E + P) v_j) &= \frac{\partial}{\partial x_j} (\varpi_{ij} v_i - q_j) \end{aligned} \quad (57)$$

for $i = 1, \dots, d$. The density of the fluid $\rho : \Omega \rightarrow \mathbb{R}_{>0}$, the fluid velocity $v : \Omega \rightarrow \mathbb{R}^d$, and the total energy of the fluid $\rho E : \Omega \rightarrow \mathbb{R}_{>0}$ are implicitly defined as the solution of (57). We assume the fluid is an ideal gas with thermal and caloric state equations

$$P = \rho R T, \quad e = \frac{1}{\gamma - 1} \frac{P}{\rho}, \quad (58)$$

where $P : \Omega \rightarrow \mathbb{R}_{>0}$ and $T : \Omega \rightarrow \mathbb{R}_{>0}$ are the pressure and temperature of the fluid, $e : \Omega \rightarrow \mathbb{R}_{>0}$ is the specific internal energy, $R \in \mathbb{R}_{>0}$ is the specific gas constant, and $\gamma > 1$ is the ratio of specific heats. The total energy is the sum of the internal energy and the kinetic energy

$$\rho E = \rho e + \frac{1}{2} \rho v_i v_i. \quad (59)$$

For a calorically perfect gas, the pressure is directly related to the conservative variables as

$$P = (\gamma - 1) (\rho E - \rho v_i v_i / 2). \quad (60)$$

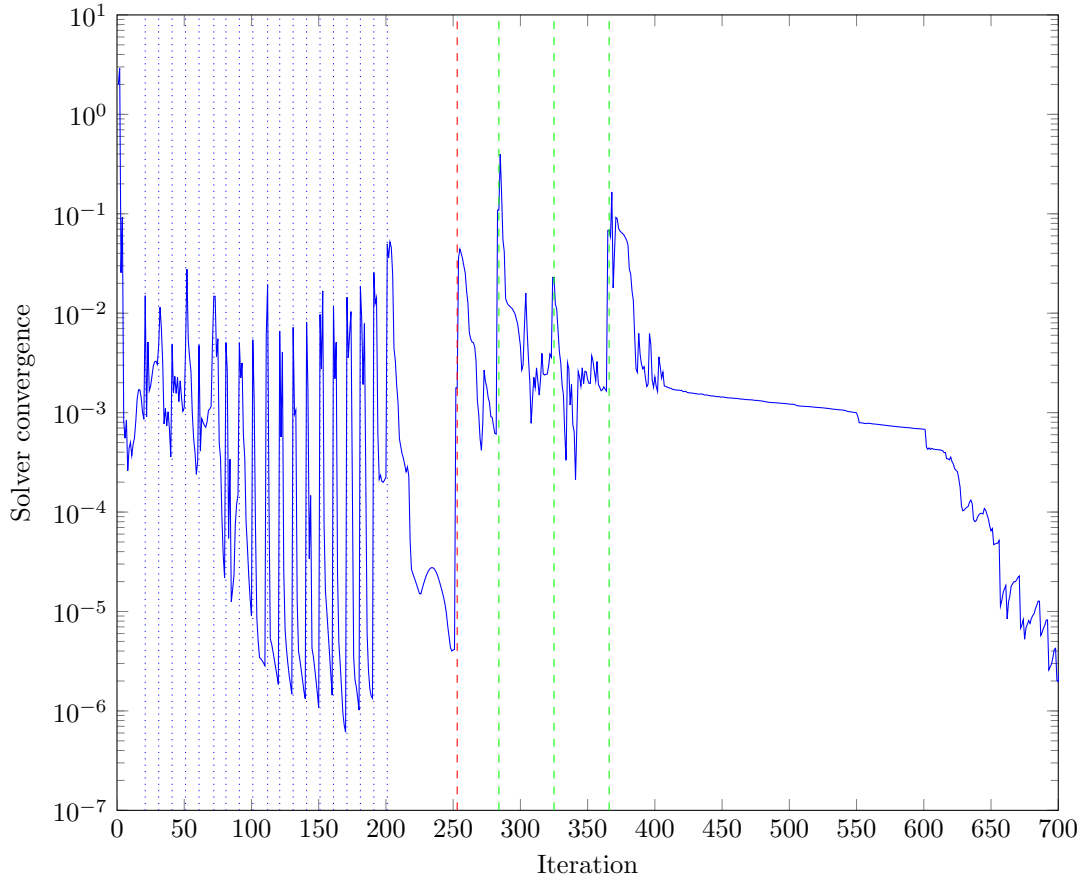


Figure 13: Convergence of the DG residual $\|\mathbf{r}^{(j)}(\mathbf{u}_k^{(j)}, \phi(\mathbf{y}_k^{(j)}); \Xi_i)\|$ (—) across all viscosity continuation stages $\{\Xi_i\}_{i=1}^{20}$ and p -adaptivity iterations $\{p_j\}_{j=0}^3$. Vertical lines indicate the end of a continuation state (---) (i.e., transition from Ξ_i to Ξ_{i+1}) or the end of a p -adaptation iteration (---) (i.e., transition from p_j to p_{j+1}) for the viscous Burgers' problem with curved shock.

Assuming a Newtonian fluid with heat transfer that obeys Fourier’s law, the shear stress, $\varpi : \Omega \rightarrow \mathbb{R}^{d \times d}$, and heat flux, $q : \Omega \rightarrow \mathbb{R}^d$, are related to the primitive flow variables as

$$\varpi_{ij} = \mu \left(\frac{\partial v_i}{\partial x_j} + \frac{\partial v_j}{\partial x_i} - \frac{2}{3} \frac{\partial v_k}{\partial x_k} \delta_{ij} \right), \quad q_i = -\kappa \frac{\partial T}{\partial x_i}, \quad (61)$$

where $\mu : \Omega \rightarrow \mathbb{R}_{>0}$ is the dynamic viscosity (independent of the fluid state by assumption), and $\kappa : \Omega \rightarrow \mathbb{R}_{>0}$ is the thermal conductivity. We use a constant viscosity model $\mu = \text{Pr} \cdot \kappa / c_P$, where $\text{Pr} \in \mathbb{R}_{>0}$ is the Prandtl number and $c_P \in \mathbb{R}_{>0}$ is the specific heat capacity at constant pressure.

4.2.1. Flow over a laminar flat plate: rp - vs. h -adaptation study

In this problem, we consider flow over a flat plate to demonstrate the ability of the rp -adaptive method to resolve boundary layers, and compare it side-by-side to a high-order, anisotropic h -adaptation method. For this study, we consider a nondimensional version of the flat plate problem from [16], nondimensionalized with respect to static inlet conditions (density, sound speed, temperature) and the length of the flat plate. The inlet Mach number is $M_\infty = 0.2$, the target Reynolds number is $\text{Re} = 1301233.166$, the ratio of specific heats is $\gamma = 1.4$, and the Prandtl number is $\text{Pr} = 0.72$. The boundary conditions are summarized in Figure 14. The flow angle, stagnation temperature, and pressure are prescribed at the inlet ($v/\|v\|_2 = (1, 0)$, $P_0 = 0.7345$, $T_0 = 1.008$), the static pressure is prescribed at the outlet ($P_{\text{out}} = 0.7143$), and the flat plate is modeled as an adiabatic no-slip condition. Additionally, a homogeneous normal viscous flux is imposed on the inlet and outlet boundaries.

We discretize the domain using a structured, uniform 30×10 grid of straight-sided ($q = 1$) quadrilateral elements with quadratic solution approximation ($p_0 : K \mapsto 2$). The HOIST solver is initialized from the DG solution on this coarse discretization (Figure 15). To ensure the boundary layer is properly emphasized, we use the element scaling in Section 3.5.3 with $\lambda = 100$. Reynolds number continuation is performed in 15 stages of equal increments beginning with $\Xi_1 = 10^4$ and ending with $\Xi_{15} = 1301233.166$ with each continuation stage allotted 20 SQP iterations. We use step length modifications based on the density and pressure with $\theta_1 = 0.1$ and $\theta_u = 10$ (Section 3.5.4); PTC-based step modifications with $\epsilon = 0.9$, $n_{\text{ptc}} = 5$, and $\omega_{\text{mod}} = 5$ (Section 3.5.5); and enriched residual-based Hessian regularization with $C_1 = 1$, $C_u = 10$, $\eta_1 = 0.8$, $\eta_2 = 1$, and $\hat{\gamma} = 10^4$ (Section 3.5.6). Finally, the enrichment degree is $\Delta = 2$ and we perform four rounds of p -refinement using the dual-weighted residual error indicator based on the drag on the flat plate.

During the continuation procedure, mesh elements are compressed toward the leading edge singularity and two layers of elements are squeezed near the boundary layer. The p -refinement process concentrates the highest degrees near the leading edge singularity and the beginning of the flat plate where the boundary layer is thinnest. The boundary layer at the end of the plate is well-resolved with a single element of moderate degree (Figure 16). From this figure, we also see the p -refinement process effectively reduces the magnitude of the error indicator across the domain. The internal structure of the boundary layer, as well as the distribution of error and polynomial degree, are more clear when visualized on the reference domain Ω_0 because the boundary layer is expanded (Figure 17). From these figures, we see the proposed rp -adaptive method successfully morphs a uniform mesh into one with substantial refinement, both in terms of element size and polynomial degree, in the boundary layer and near the leading edge singularity. Furthermore, after four p -refinement cycles, the boundary layer profile and skin friction coefficient closely agree with the Blasius solution (Figure 18) (the profile agrees after only three adaptation cycles).

Finally, we compare the proposed rp -adaptive method to an anisotropic h -adaptive method. The h -adaptive method uses $p = 1, 2$, and 3 discretizations, with the initial uniform mesh comprised 15×5 elements. For both methods, error adaptation is driven by the dual-weighted residual error estimate based on the flat plate drag. Both methods reach a solution with sub-1% error; however, the proposed rp -adaptive method requires more degrees of freedom than the h -adaptive method to achieve such a solution for all polynomial degrees considered (Figure 19). A representative example of the h -adapted mesh and solution produced by the h -adaptive method is provided in Figure 20. While this method demonstrated the flexibility of the proposed method to automatically adapt a uniform mesh to boundary layers, it is not necessarily competitive with other approaches. In the next section, we show that it is highly competitive for flows involving strong shocks.

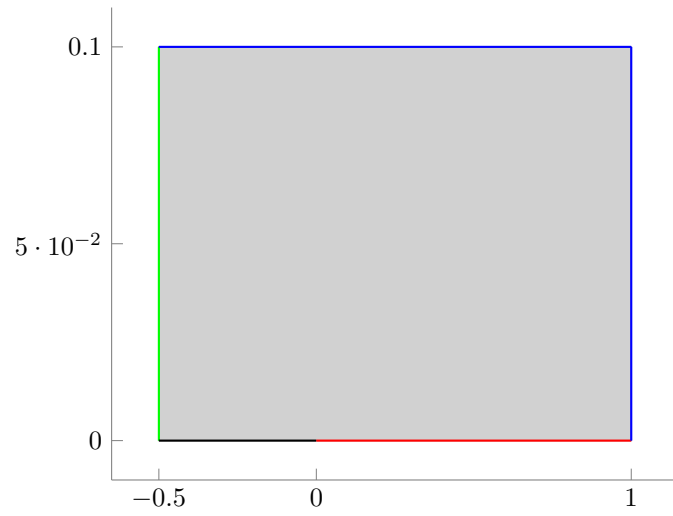


Figure 14: Schematic of flat plate domain and boundary conditions. Boundary conditions: subsonic inlet (—), subsonic outlet (—), adiabatic no-slip wall (—), symmetry condition (—).

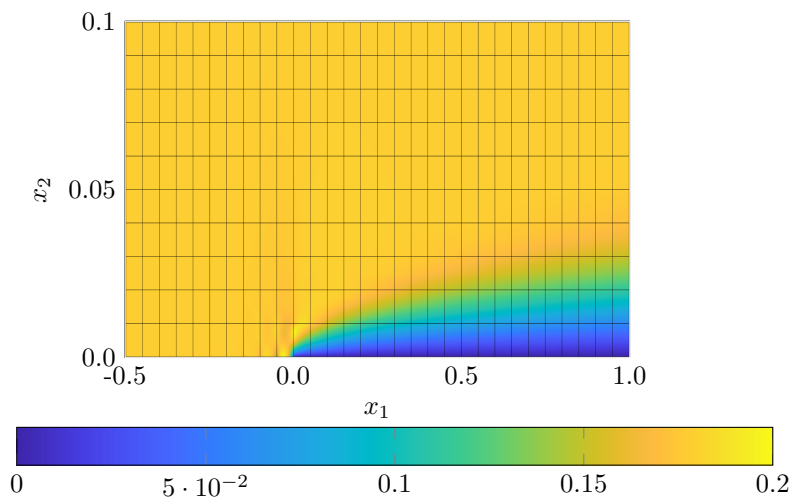


Figure 15: Mesh and solution (DG solution with $\text{Re} = 10^4$) used to initialize the rp -adaptive HOIST method for the flat plate problem.

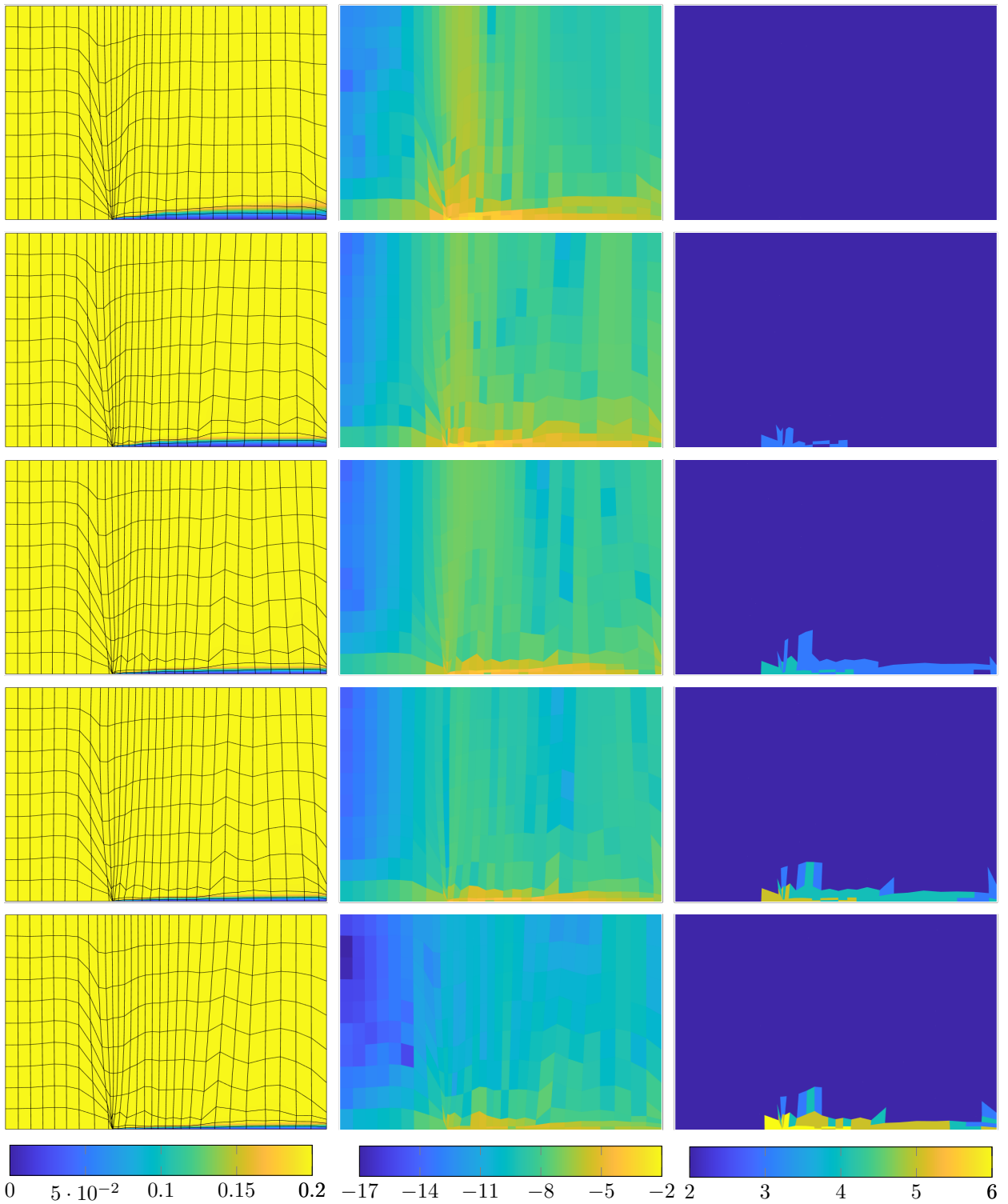


Figure 16: HOIST solution (rp -adaptation) (Mach number) (*left*), the drag-based dual-weighted residual error estimate (*middle*), and the polynomial degree distribution (*right*) in the physical domain $\mathcal{G}(\Omega_0)$ to the flat plate problem. These quantities are provided prior to p -adaptation and after each p -adaptation iteration (*top-to-bottom*).

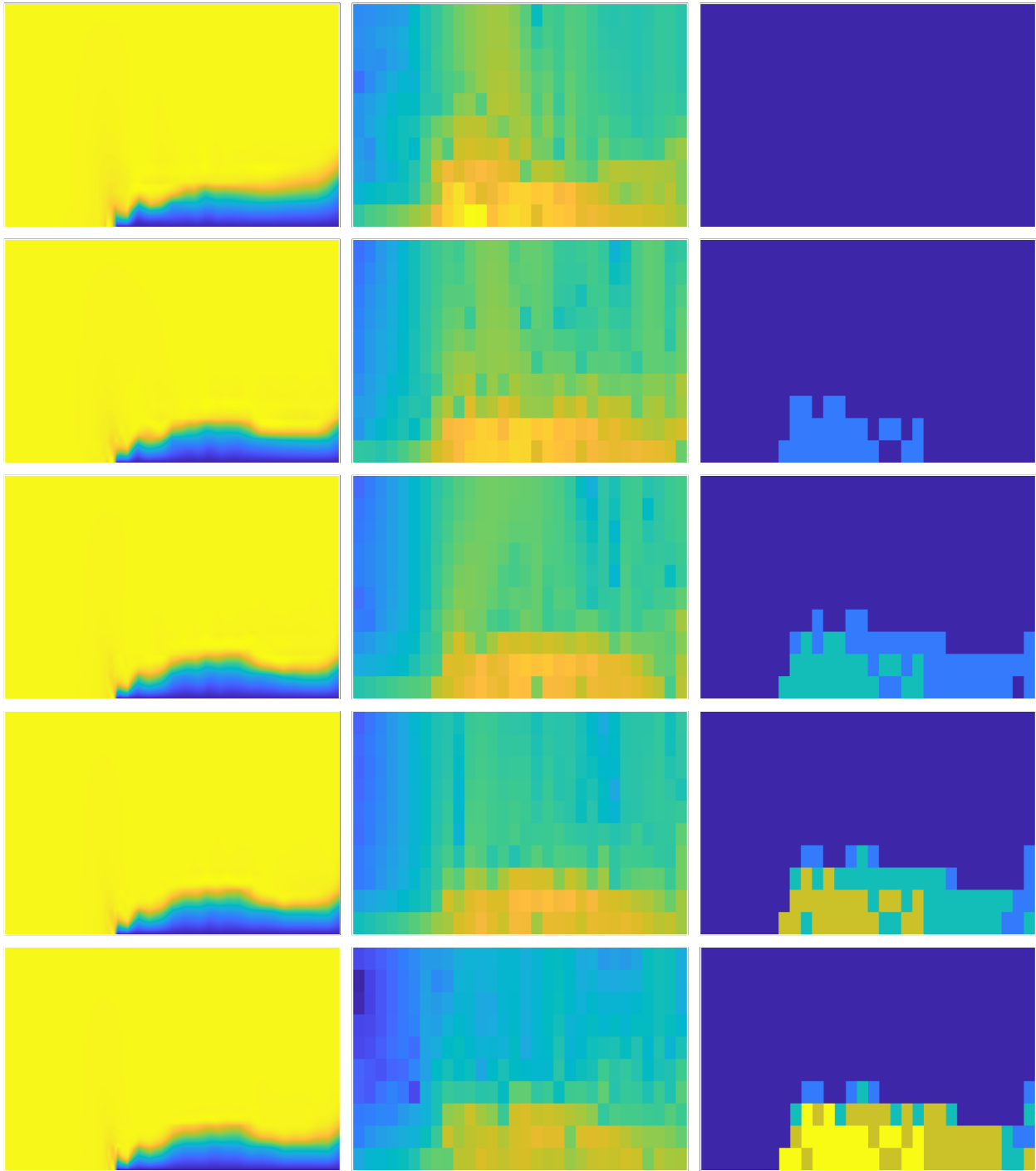


Figure 17: HOIST solution (rp -adaptation) (Mach number) (*left*), the drag-based dual-weighted residual error estimate (*middle*), and the polynomial degree distribution (*right*) in the reference domain to the flat plate problem. These quantities are provided prior to p -adaptation and after each p -adaptation iteration (*top-to-bottom*). Colorbar in Figure 16.

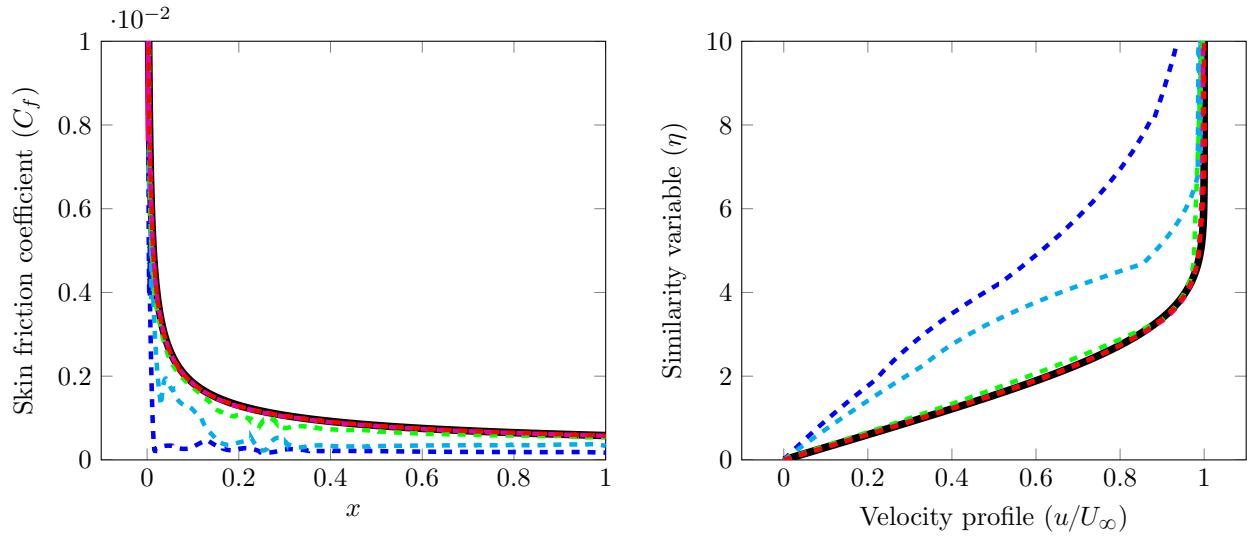


Figure 18: The skin friction coefficient (*left*) and boundary layer profile (*right*) computed from the Blasius solution (—) and the HOIST solution (*rp*-adaptation) prior to p -adaptation (---) and after the first (---), second (---), third (---), and fourth (---) p -adaptation iterations for the flat plate problem.

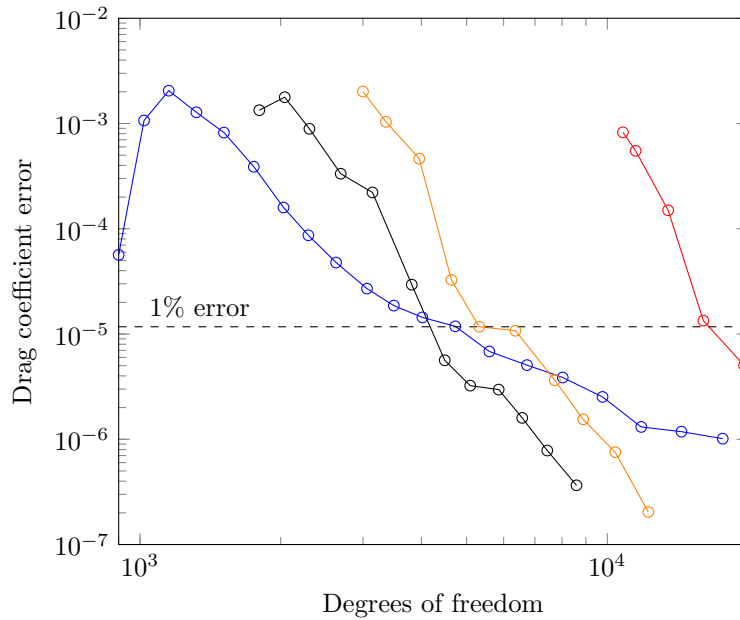


Figure 19: Convergence of the error in the drag coefficient for the HOIST method (*rp*-adaptation) (—○—) and the h -adaptive method with linear (—○—), quadratic (—○—), and cubic (—○—) constant polynomial degree for the flat plate problem. Both flow and mesh degrees of freedom are counted the HOIST method ($N_{\mathbf{u}}^{(j)} + N_{\mathbf{x}}$), while only flow degrees of freedom are present for the h -adaptive method.

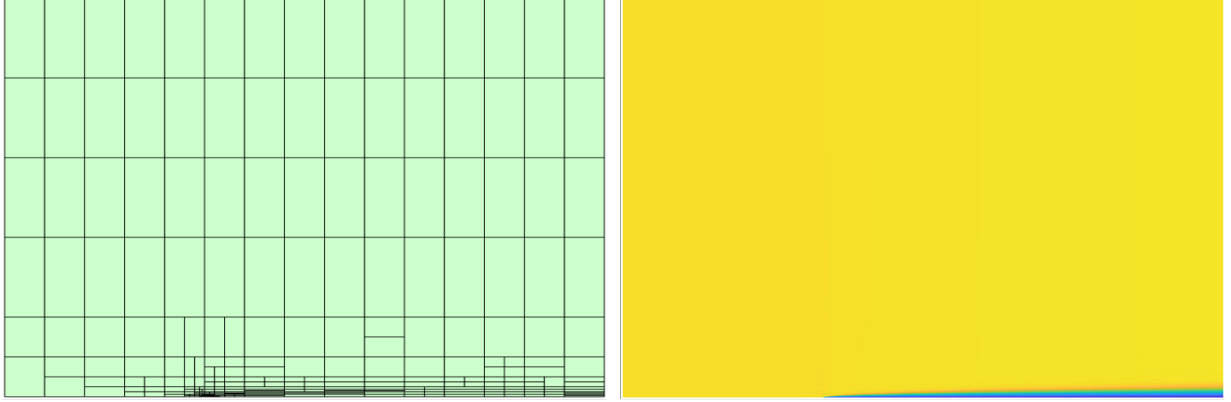


Figure 20: The h -adapted mesh (*left*) and corresponding solution (Mach number) (*right*) for the flat plate problem using drag-based dual-weighted residual adaptation used for the comparative study with the HOIST method (rp -adaptation).

4.2.2. Hypersonic flow over cylinder: rp - vs. h -adaptation study

In this problem, we consider hypersonic flow over a cylinder to demonstrate the ability of the rp -adaptive method to accurately resolve a strong, thin bow shock and thin boundary layer, and compare it side-by-side to a high-order, anisotropic h -adaptive method. For this study, we consider the problem in [31] in a slightly modified computational geometry with cylinder wall defined as the unit circle and the farfield boundary defined as the ellipse $(x_1/6)^2 + (x_2/3)^2 = 1$. The inlet Mach number is $M_\infty = 5$, the target Reynolds number based on the radius of the cylinder is $\text{Re} = 1000$, the ratio of specific heats is $\gamma = 1.4$, the Prandtl number is $\text{Pr} = 0.72$, and the isothermal wall temperature is $T_w/T_\infty = 2.5$. The geometry and boundary conditions are illustrated in Figure 21. The entire primitive state is prescribed at the supersonic inlet and the cylinder wall is modeled as an isothermal no-slip condition. Additionally, a homogeneous normal viscous flux is imposed on the inlet and outlet boundaries.

We discretize the domain using a structured, uniform mesh of 210 curved ($q = 2$) quadrilateral elements with quadratic solution approximation ($p_0 : K \mapsto 2$). The HOIST solver is initialized from a shock capturing DG solution using PDE-based artificial viscosity from [4] on this coarse discretization (Figure 22). To ensure the boundary layer is properly emphasized, we use the element scaling in Section 3.5.3 with $\lambda = 10$. Reynolds number continuation is performed in 10 stages of equal increments beginning with $\Xi_1 = 10^2$ and ending with $\Xi_{10} = 10^3$ with the first continuation stage allotted 40 SQP iterations and the remaining stages allowed 20 SQP iterations. We use step length modifications based on the density and pressure with $\theta_1 = 0.1$ and $\theta_u = 10$ (Section 3.5.4); PTC-based step modifications with $n_{\text{ptc}} = 5$, $\epsilon = 0.9$, and $\omega_{\text{mod}} = 10$ (Section 3.5.5); and enriched residual-based Hessian regularization with $C_1 = 1$, $C_u = 10$, $\eta_1 = \eta_2 = 1$, and $\hat{\gamma} = 100$ (Section 3.5.6). Finally, the enrichment degree $\Delta = 2$ is used and we perform five rounds of p -refinement using the enriched residual error indicator. After all SQP iterations are exhausted in the final p -adaptation iteration, PTC is used to drive the DG residual to $\mathcal{O}(10^{-9})$ in less than 20 time steps using the (now fixed) rp -adapted approximation space without any form of nonlinear stabilization.

During the continuation procedure, mesh elements are compressed toward the bow shock and boundary layer with the compression being particularly tight in the vicinity of the stagnation streamline. Interestingly, the p -refinement process concentrates the highest polynomial degrees in the bow shock, moderate degrees between the bow shock and boundary layer, and lowest degrees in the boundary layer (Figure 23). The lower degrees in the boundary layer are likely due to the extremely tight grid spacing (due to r -adaptation) making them sufficient to resolve the feature, and from our choice to use the unweighted enriched residual indicator. This figure also shows the p -refinement process effectively reduces the magnitude of the error indicator across the domain. The internal structure of the bow shock and boundary layer, as well as the distribution of error and polynomial degree, are more clear when visualized on the reference domain Ω_0 because the thin features are expanded (Figure 24). From these figures, we see the proposed rp -adaptive method successfully morphs a structured mesh into one with substantial refinement, in terms of element size and/or polynomial degree, near the shock and boundary layer. Furthermore, after five p -refinement cycles, the heat flux profile, a notoriously difficult quantity to predict, is well-resolved (Figure 25); however,

the combination of r - and p -adaptivity was crucial as r -refinement alone and early p -refinement iterations produce a highly oscillatory heat flux profile with substantial inter-element jumps. Finally, it is interesting to note that the heat flux computed from the lifted viscous flux (σ) provides a smoother profile with smaller inter-element jumps than direct differentiation (Figure 26); see discussion in Remark 3.

Next, we compare the proposed rp -adaptive method to a high-order h -adaptive method with adaptation driven by the dual-weighted residual error estimate based on the integrated heat flux over the cylinder. The h -adaptive method uses $p = 1, 2,$ and 3 discretizations and the same initial mesh as the rp -adaptive method. Both methods achieve solutions with sub-1% error, and the proposed rp -adaptive method requires fewer degrees of freedom than the h -adaptive method to do so (Figure 27). This shows the HOIST method with rp -adaptive method effectively resolves complex high-speed flow features and achieves high accuracy per degree of freedom, making it a competitive approach for such problems. A representative example of the h -adapted mesh and solution produced by the h -adaptive method is provided in Figure 28. The DWR method refines the shock only in the regions relevant to the heat flux evaluation.

The behavior of the SQP solver across all continuation and p -adaptation stages is shown in Figure 29. For a given value of the viscosity Ξ_i and polynomial distribution p_j , the HOIST method drives the residual toward zero. However, the residual jumps up after the continuation parameter or polynomial distribution is updated because the residual function changes. Notice that 260 iterations are performed on the coarsest (i.e., least expensive) discretization that uses a quadratic approximations in all elements. The p -adaptation process is complete in another 160 iterations, at which point the mesh is effectively frozen. After the SQP iterations are complete, PTC is used to deeply converge the residual on a fixed mesh to a tolerance of 10^{-9} .

The remainder of this section studies the impact of the various aspects of the complete rp -adaptive HOIST formulation and solver.

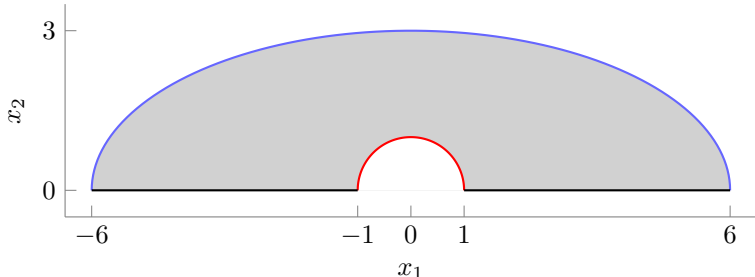


Figure 21: Schematic of cylinder domain and boundary conditions. Boundary conditions: supersonic inlet (—), supersonic outlet (—), isothermal no-slip wall (—).

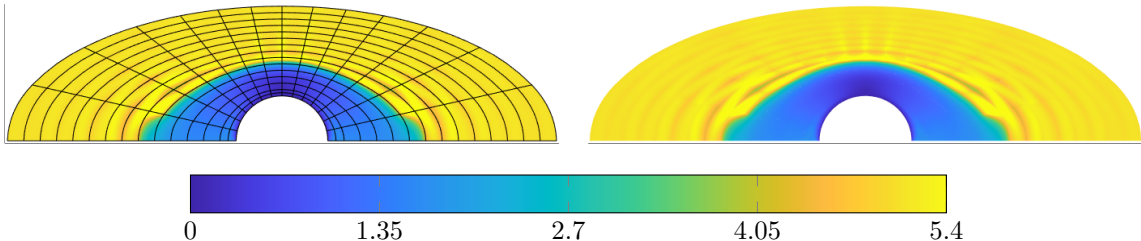


Figure 22: Mesh and solution (shock capturing for $\text{Re} = 10^2$) used to initialize the rp -adaptive HOIST method for the cylinder problem.

4.2.3. Hypersonic flow over cylinder: importance of Reynolds continuation

In this section, we consider the hypersonic cylinder problem in Section 4.2.2 and demonstrate the importance of Reynolds number continuation with all other solver and formulation parameters identical to those in Section 4.2.2. Without Reynolds number continuation, i.e., HOIST is directly applied to the target Reynolds number $\Xi_1 = \text{Re} = 1000$, carbuncle phenomena [42, 44] arise, which are particularly detrimental in an r -adaptation setting because the mesh tracks the forming carbuncle (Figure 30).

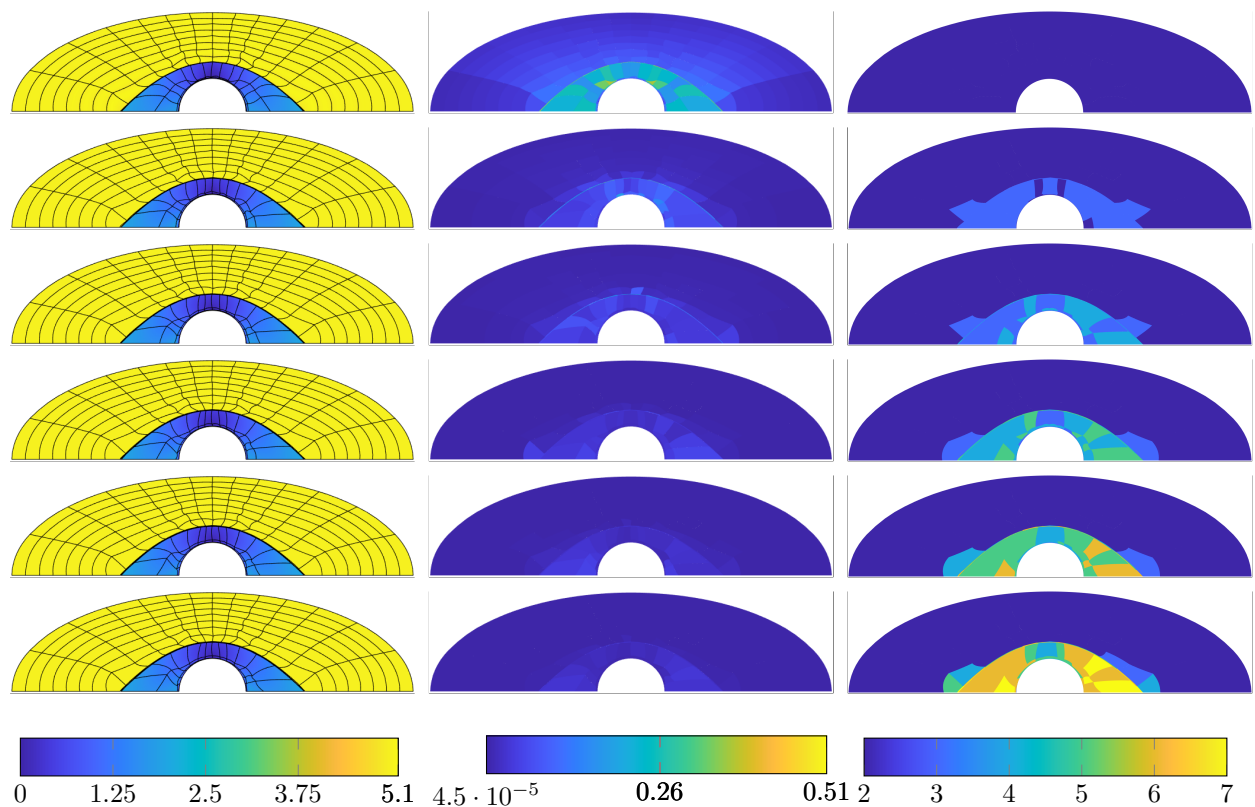


Figure 23: HOIST solution (rp -adaptation) (Mach number) (*left*), the enriched residual error estimate (*middle*), and the polynomial degree distribution (*right*) in the physical domain $\mathcal{G}(\Omega_0)$ to the cylinder problem. These quantities are provided prior to p -adaptation and after each p -adaptation iteration (*top-to-bottom*).

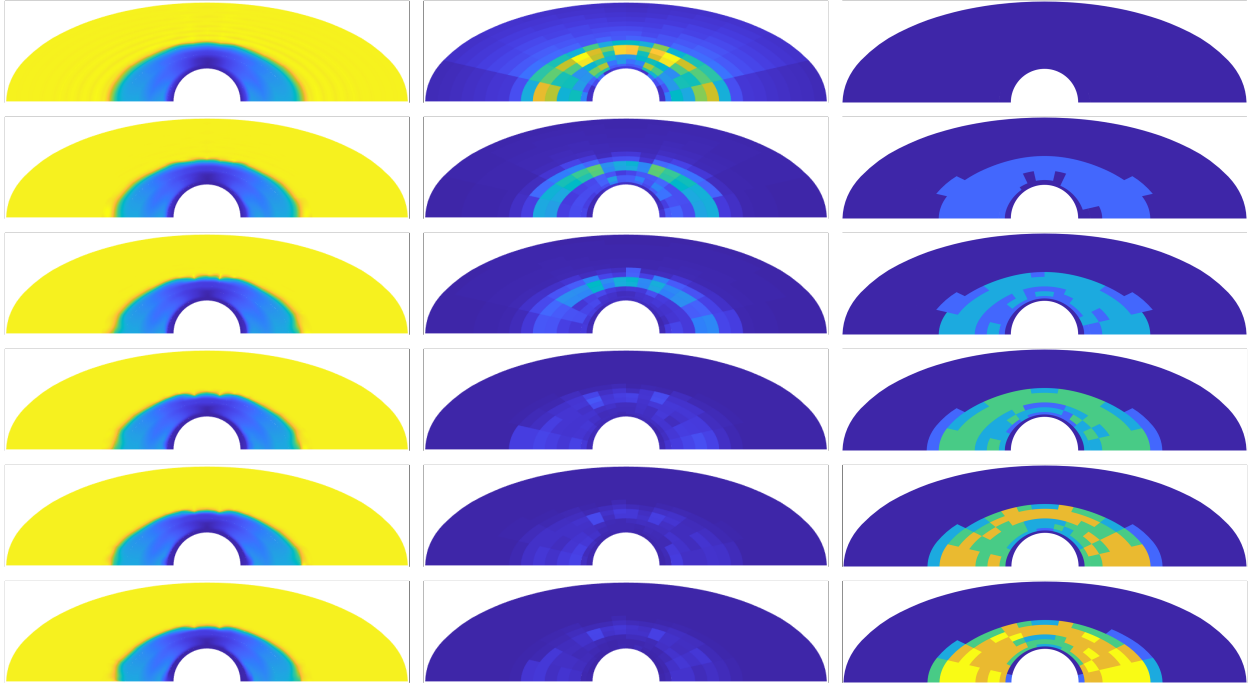


Figure 24: HOIST solution (rp -adaptation) (Mach number) (*left*), the enriched residual error estimate (*middle*), and the polynomial degree distribution (*right*) in the reference domain to the cylinder problem. These quantities are provided prior to p -adaptation and after each p -adaptation iteration (*top-to-bottom*). Colorbar in Figure 23.

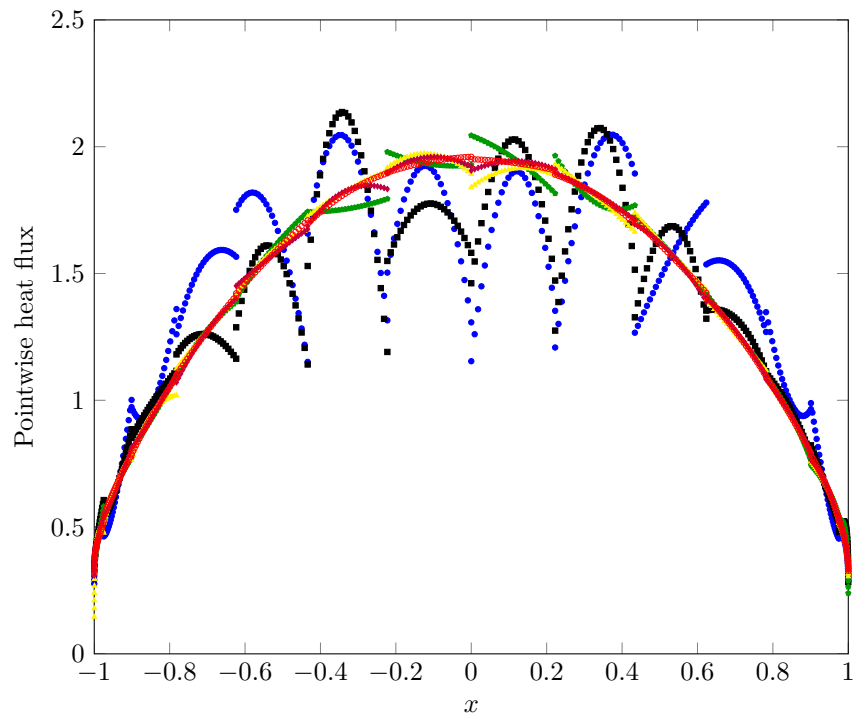


Figure 25: Pointwise heat flux over the cylinder surface computed from the HOIST solution (rp -adaptation) prior to p -adaptation (\bullet) and after the first (\blacktriangle), second (\circ), third (\triangle), fourth (\blacklozenge), and fifth (\circ) p -adaptation iteration.

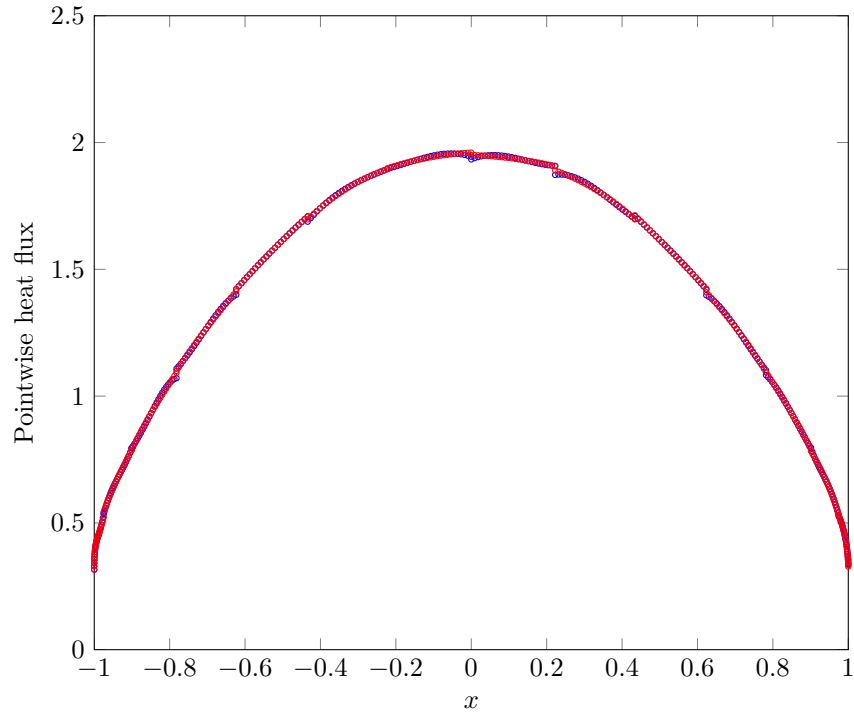


Figure 26: Pointwise heat flux profile over the cylinder surface computed from the HOIST solution (rp -adaptation) based on lifted viscous flux (●) and via direct differentiation (●) (Remark 3) after fifth p -adaptation iteration.

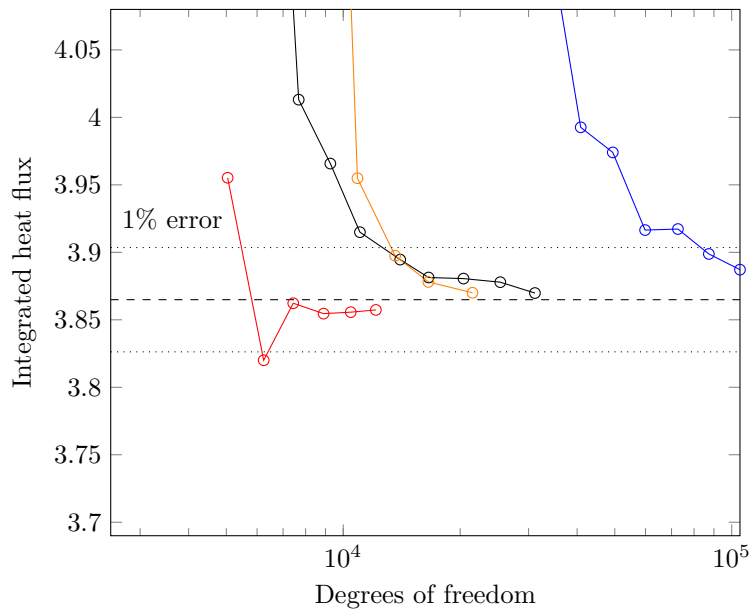


Figure 27: Convergence of the integrated heat flux for the HOIST method (rp -adaptation) (—●—) and the h -adaptive method with linear (—●—), quadratic (—●—), and cubic (—●—) constant polynomial degree for the cylinder problem. Both flow and mesh degrees of freedom are counted for the HOIST method ($N_{\mathbf{u}}^{(j)} + N_{\mathbf{x}}$), while only flow degrees of freedom are present for the h -adaptive method.

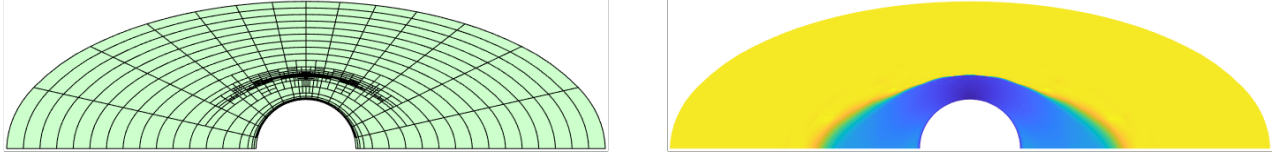


Figure 28: The h -adapted mesh (*left*) and corresponding solution (Mach number) (*right*) for the cylinder problem using integrated heat flux-based dual-weighted residual adaptation used for the comparative study with the HOIST method (rp -adaptation).

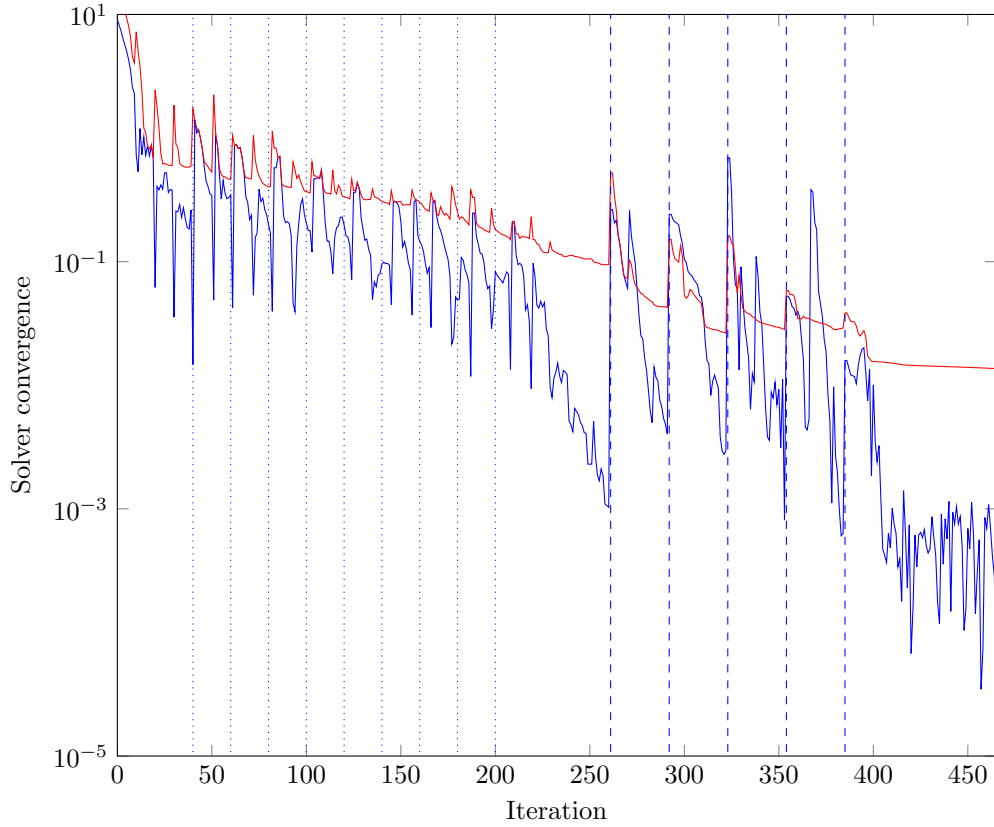


Figure 29: Convergence of the DG residual $\|\mathbf{r}^{(j)}(\mathbf{u}_k^{(j)}, \boldsymbol{\phi}(\mathbf{y}_k^{(j)}); \Xi_i)\|$ (—) and enriched DG residual $\|\mathbf{R}_\rho^{(j)}(\mathbf{u}_k^{(j)}, \boldsymbol{\phi}(\mathbf{y}_k^{(j)}); \Xi_i)\|$ (—) across all Reynolds number continuation stage $\{\Xi_i\}_{i=1}^{10}$ and p -adaptivity iterations $\{p_j\}_{j=0}^5$. Vertical lines indicate the end of a continuation stage (.....) (i.e., transition from Ξ_i to Ξ_{i+1}) or the end of a p -adaptation iteration (- - -) (i.e., transition from p_j to p_{j+1}) for the cylinder problem.

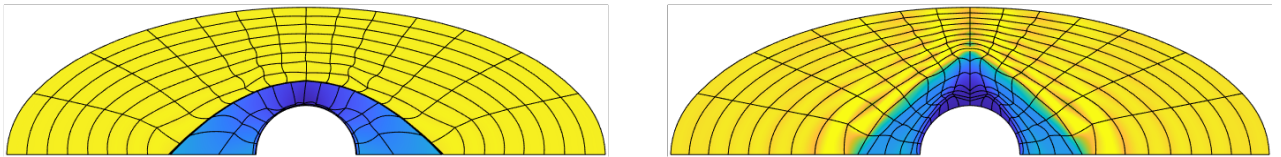


Figure 30: HOIST solution (Mach number) (r -adaptation) with the Reynolds number continuation strategy of Section 3.3 (*left*) and without continuation ($\Xi_1 = \text{Re} = 1000$) (*right*) for the cylinder problem. Colorbar in Figure 22.

4.2.4. Hypersonic flow over cylinder: impact of enrichment degree

Next, we consider the hypersonic cylinder problem in Section 4.2.2 and demonstrate the impact of the enrichment degree Δ . In particular, we compare the choice $\Delta = 1$ to the $\Delta = 2$ choice used throughout this work with all other solver parameters identical to those in Section 4.2.2. We find that $\Delta = 1$ leads to substantially less mesh compression in the boundary layer (Figure 31) and worse prediction of the heat flux profile (Figure 32).

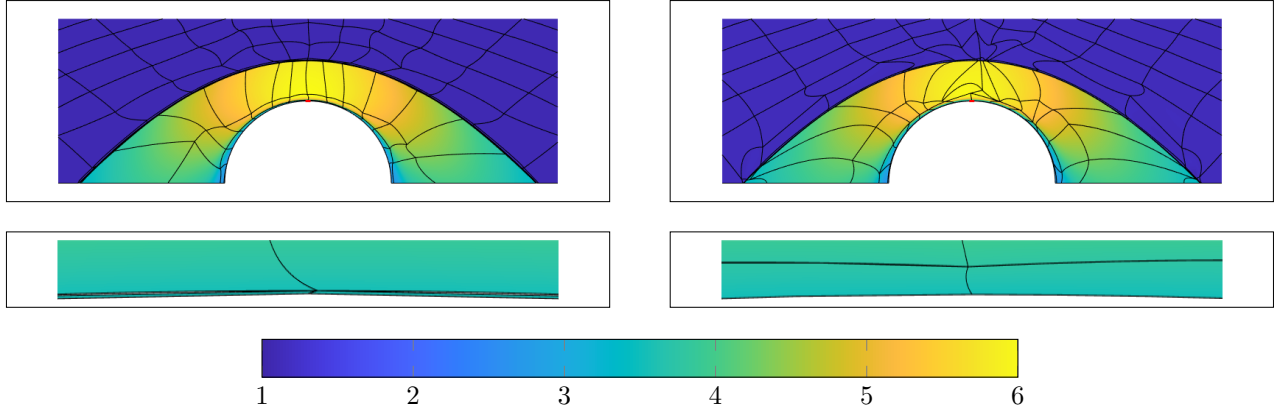


Figure 31: HOIST solution (temperature) (rp -adaptation) based on test space enrichment $\Delta = 2$ (left) and $\Delta = 1$ (right) for the cylinder problem.

4.2.5. Hypersonic flow over cylinder: impact of boundary residual weighting

Next, we consider the hypersonic cylinder problem in Section 4.2.2 and demonstrate the impact of boundary residual weighting λ . In particular, we compare the choice $\lambda = 1$ (unweighted) to the $\lambda = 10$ choice used in Section 4.2.2. All other solver parameters are identical to those in Section 4.2.2. We find that the unweighted scenario does not sufficiently compress the mesh to resolve the boundary layer (Figure 33), which leads to inaccurate heat flux profiles (Figure 34).

4.2.6. Hypersonic flow over cylinder: p -adaptation error indicator

Finally, we consider the hypersonic cylinder problem in Section 4.2.2 and demonstrate the performance of the HOIST method (rp -adaptation) with different error indicators driving p -adaptation. All of the solver parameters are identical to those in Section 4.2.2. The dual-weighted residual error indicator based on the integrated heat flux concentrates the highest polynomial degrees near the stagnation line, whereas the feature-based sensor based on the magnitude of the velocity gradient only enriches the polynomial degree in the shock layer (Figure 35).

The distribution of polynomial degree produced by the dual-weighted residual sensor is not ideal because the lowest polynomial degree (two) is used in the lateral regions (minor contributions to the integrated heat flux), which means r -adaptation alone is used to resolve the bow shock in these regions. Regardless, the integrated heat flux reaches sub-1% error using this trial space, which is not surprising because the polynomial distribution is tailored to accurately predict this quantity of interest. However, because the shock is not adequately resolved, the PTC solver fails to deeply converge the solution without additional stabilization. The dual-weighted residual method is known to be more effective than residual-based methods for approximating quantities of interest [5, 18]. However, in the present formulation, mesh optimization plays a role of improving not just accuracy by providing better approximation spaces but also stability by providing shock-aligned meshes. The former is desired, but the latter is required; the dual-weighted residual method by construction accounts for the former but not the latter, and hence is not best suited for the present formulation.

Furthermore, the distribution of polynomial degree produced by the feature-based sensor is suboptimal despite highly focusing the p -refinement in the bow shock because (1) the boundary layer is not being refined

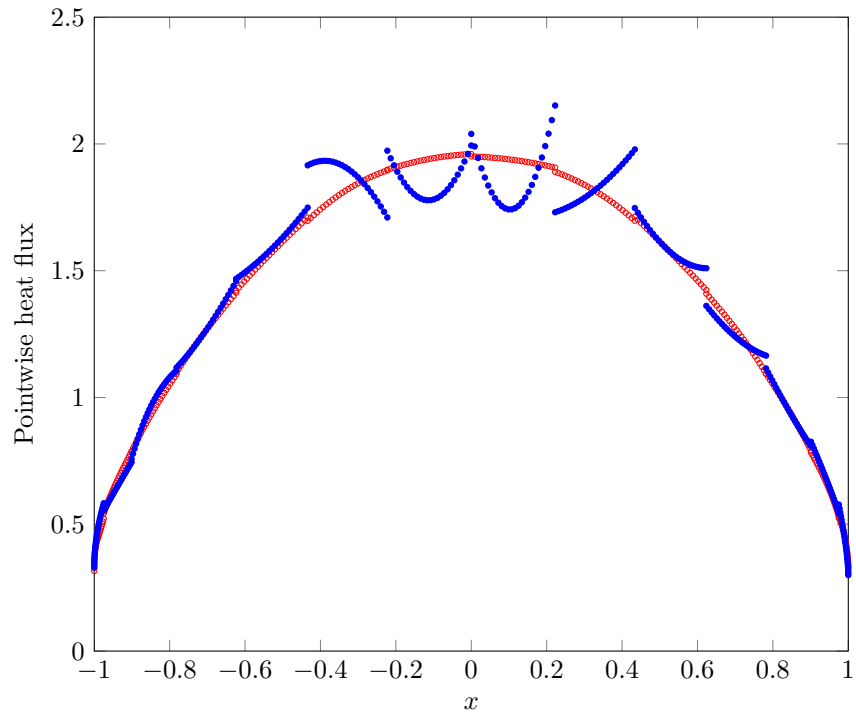


Figure 32: Pointwise heat flux profile over the cylinder surface computed from the HOIST solution (*rp*-adaptation) based on test space enrichment $\Delta = 2$ (◦) and $\Delta = 1$ (•).

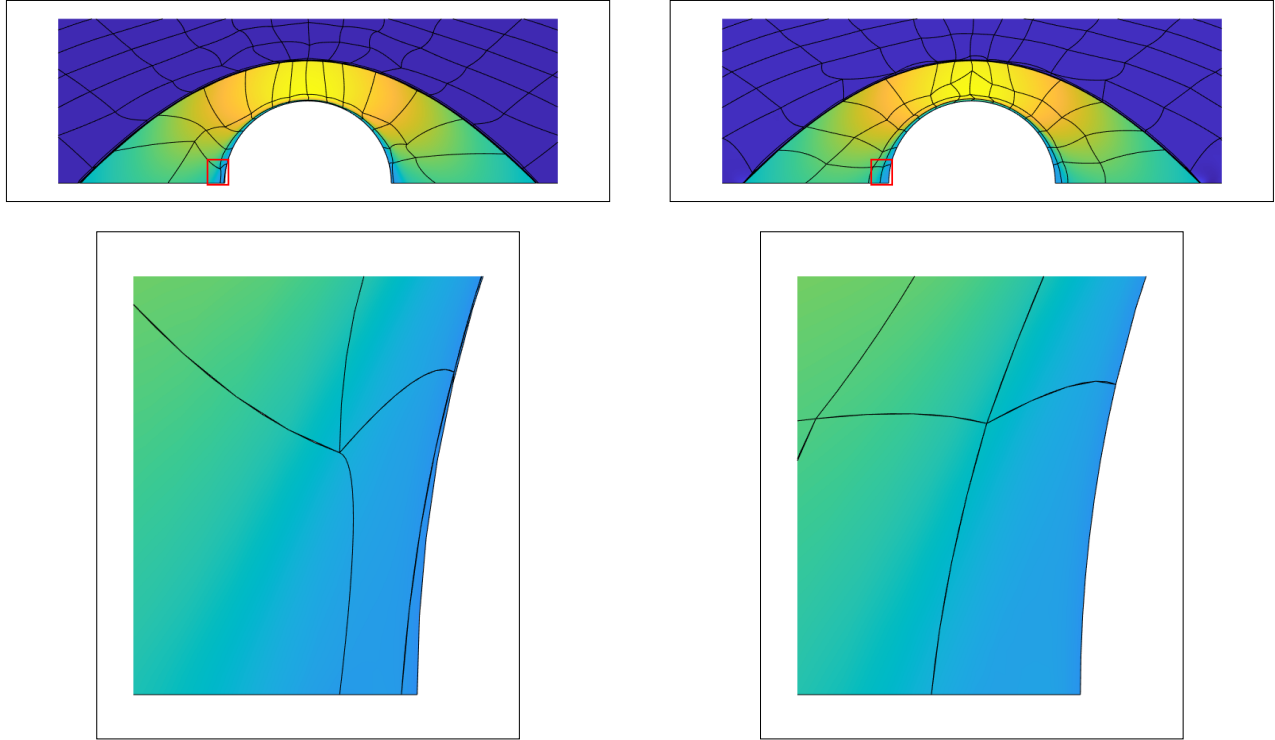


Figure 33: HOIST solution (temperature) (*rp*-adaptation) based on boundary residual scaling $\lambda = 10$ (*left*) and $\lambda = 1$ (*unweighted*) (*right*). Colorbar in Figure 31.

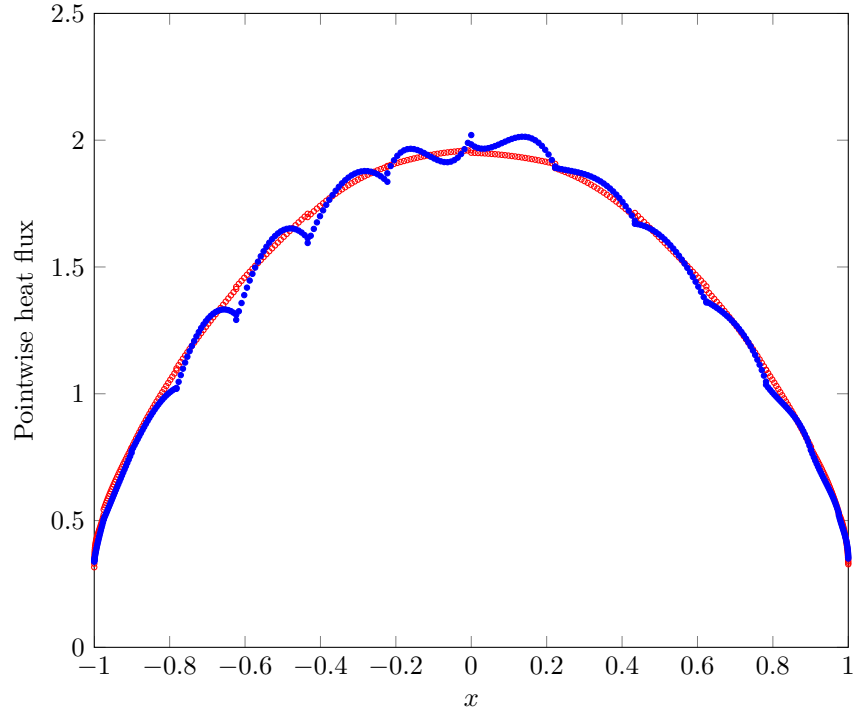


Figure 34: Pointwise heat flux profile over the cylinder surface computed from the HOIST solution (*rp*-adaptation) based boundary residual scaling $\lambda = 10$ (\circ) and $\lambda = 1$ (unweighted) (\bullet).

and (2) the bow shock will always be targeted for refinement, even once it has been adequately resolved due to the use of a feature-based (not error-based) sensor. Unlike the trial space produced from the dual-weighted residual indicator, the integrated heat flux is inaccurate using this feature-adapted trial space due to lack of boundary layer refinement. However, deep convergence using PTC is obtained because the shock is adequately resolved.

The enriched residual sensor used in Section 4.2.2 combines the best aspects of the other two sensors. It is an error-based sensor so refinement will be placed where resolution is needed, regardless of the steepness of the features. This ensures sufficient refinement will be placed in both the shock and boundary layer; the former enables deep convergence using PTC without stabilization and the latter leads to accurate heat flux calculations.

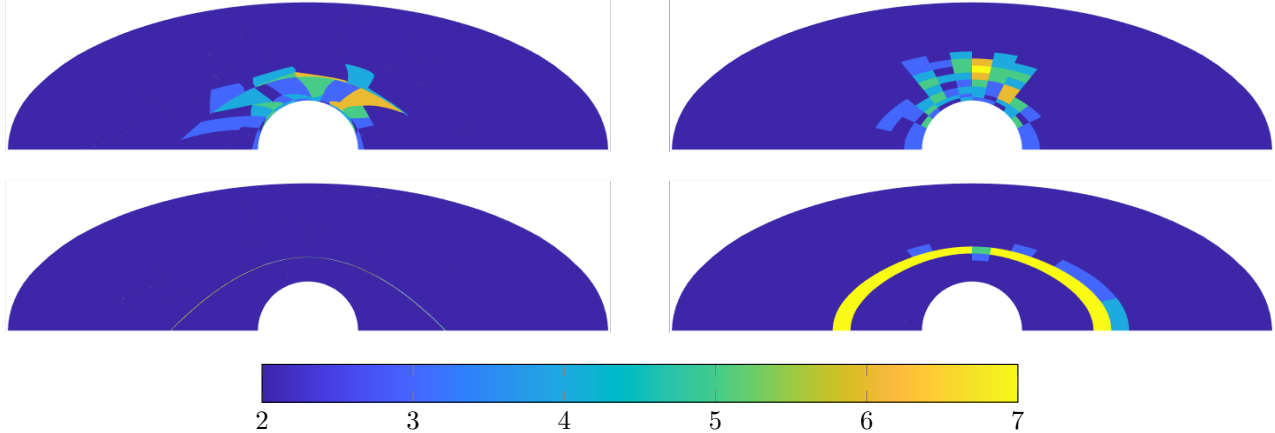


Figure 35: Distribution of the polynomial degree for the HOIST method (rp -adaptation) after five p -adaptation iterations using the dual-weighted residual sensor \hat{s}^{dwr} based on the integrated heat flux quantity (*top*) and the magnitude of the velocity gradient \hat{s}^{fbs} (*bottom*). The sensors are provided on the physical domain (*left*) and reference domain (*right*) for clarity.

5. Conclusion

In this work, we extended the implicit shock tracking method of [51, 53, 26] from a method that automatically aligns element faces with discontinuities in the solution field to one that resolves strong, rapid transitions (e.g., viscous shock waves and boundary layers) using aggressive rp -adaptivity. While both approaches share the same optimization formulation, several key innovations were necessary to resolve the viscous features. First, an appropriate discretization for a second-order conservation law is required (we use IPDG in this work). Second, an objective function corresponding to a test space enriched by two polynomial degrees led to higher quality solutions and meshes than the standard approach of enriching by a single polynomial degree. Third, the incorporation of viscosity continuation was critical for extreme yet robust compression of elements into transitions and to avoid carbuncles. Fourth, p -adaptivity was used to locally increase the polynomial degree in the regions with the most error, which limited the amount of mesh compression necessary. Fifth, an artificial elemental weighting was applied to the residual of the objective function to ensure the boundary layer was prioritized equally to the shock in the objective function. Finally, a host of other measures were incorporated to improve robustness of the solver, including constraints and modifications to the SQP step and strategies to regularize the objective function Levenberg–Marquardt Hessian approximation. A collection of numerical experiments show the new HOIST method effectively resolves both shock waves and boundary layers in viscous shock-dominated flows and compares favorably in terms of accuracy per degree of freedom to aggressive h -adaptation with high-order methods. Furthermore, the rp -adaptive approach effectively predicts the heat flux profile produced by hypersonic flow over a cylinder.

Relevant future research includes the development parallel preconditioners for the linearized optimality system to effectively leverage high-performance computing, and application of the proposed approach to realistic hypersonic flows. Another promising avenue of research is the development of an implicit shock tracking method for viscous flows that approximates strong shock waves as discontinuities. Such an approach could lead to highly accurate approximations for high Reynolds flow without the need for extreme mesh compression or p -adaptivity, and potentially use coarser grids than those used in this work.

Acknowledgments

This work is supported by AFOSR award numbers FA9550-20-1-0236, FA9550-22-1-0002, FA9550-22-1-0004, ONR award number N00014-22-1-2299, and NSF award number CBET-2338843. The content of this publication does not necessarily reflect the position or policy of any of these supporters, and no official endorsement should be inferred.

References

- [1] Douglas N. Arnold. An interior penalty finite element method with discontinuous elements. *SIAM Journal on Numerical Analysis*, 19(4):742–760, 1982.
- [2] Douglas N. Arnold, Franco Brezzi, Bernardo Cockburn, and L. Donatella Marini. Unified analysis of discontinuous Galerkin methods for elliptic problems. *SIAM Journal on Numerical Analysis*, 39(5):1749–1779, 2002.
- [3] Alessia Assonitis, Renato Paciorri, and Aldo Bonfiglioli. Numerical simulation of shock/boundary-layer interaction using an unstructured shock-fitting technique. *Computers & Fluids*, 228:105058, 2021.
- [4] Garrett E. Barter and David L. Darmofal. Shock capturing with PDE-based artificial viscosity for DGFEM: Part I. Formulation. *Journal of Computational Physics*, 229(5):1810–1827, 2010.
- [5] R. Becker and R. Rannacher. An optimal control approach to a posteriori error estimation in finite element methods. *Acta Numerica*, 10:1–102, may 2001.
- [6] Roland Becker and Rolf Rannacher. A feed-back approach to error control in finite element methods: basic analysis and examples. *East-West J. Numer. Math*, 4:237–264, 1996.
- [7] Aldo Bonfiglioli, R. Paciorri, and L. Campoli. Unsteady shock-fitting for unstructured grids. *International Journal for Numerical Methods in Fluids*, 81(4):245–261, 2016.
- [8] Graham V. Candler. Next-generation CFD for hypersonic and aerothermal flows. In *22nd AIAA Computational Fluid Dynamics Conference*, Dallas, Texas, 6/22/2015 – 6/26/2015. American Institute of Aeronautics and Astronautics, AIAA Paper 2015-3048.
- [9] Graham V. Candler, Dimitri J. Mavriplis, and Loretta Trevino. Current status and future prospects for the numerical simulation of hypersonic flows. In *47th AIAA Aerospace Sciences Meeting including The New Horizons Forum and Aerospace Exposition*, Orlando, Florida, 1/5/2009 – 1/8/2009. American Institute of Aeronautics and Astronautics, AIAA Paper 2025-153.
- [10] Graham V. Candler, Pramod K. Subbareddy, and Joseph M. Brock. Advances in computational fluid dynamics methods for hypersonic flows. *Journal of Spacecraft and Rockets*, 52(1):17–28, 2015.
- [11] Eric J. Ching, Andrew D. Kercher, and Andrew Corrigan. The moving discontinuous Galerkin method with interface condition enforcement for the simulation of hypersonic, viscous flows. *Computer Methods in Applied Mechanics and Engineering*, 427:117045, 2024.
- [12] Eric J. Ching, Yu Lv, Peter Gnoffo, Michael Barnhardt, and Matthias Ihme. Shock capturing for discontinuous Galerkin methods with application to predicting heat transfer in hypersonic flows. *Journal of Computational Physics*, 376:54–75, 2019.
- [13] Mirco Ciallella, Mario Ricchiuto, Renato Paciorri, and Aldo Bonfiglioli. Extrapolated shock tracking: bridging shock-fitting and embedded boundary methods. *Journal of Computational Physics*, 412:109440, 2020.
- [14] Andrew Corrigan, Andrew D. Kercher, and David A. Kessler. A moving discontinuous Galerkin finite element method for flows with interfaces. *International Journal for Numerical Methods in Fluids*, 89(9):362–406, 2019.
- [15] Huijing Dong, Alexander Perez-Reyes, and Matthew J. Zahr. A p -adaptive high-order implicit shock tracking method for compressible, inviscid flows. In *AIAA Science and Technology Forum and Exposition (SciTech2025)*, Orlando, Florida, 1/6/2025 – 1/10/2025. American Institute of Aeronautics and Astronautics, AIAA Paper 2025-1568.
- [16] Thomas D. Economon, Francisco Palacios, Sean R. Copeland, Trent W. Lukaczyk, and Juan J. Alonso. SU2: An open-source suite for multiphysics simulation and design. *AIAA Journal*, 54(3):828–846, 2016.

- [17] Pablo Fernandez, Cuong Nguyen, and Jaime Peraire. A physics-based shock capturing method for unsteady laminar and turbulent flows. In *2018 AIAA Aerospace Sciences Meeting*, Kissimmee, Florida, 1/8/2018 – 1/12/2018. American Institute of Aeronautics and Astronautics, AIAA Paper 2018-0062.
- [18] Krzysztof J. Fidkowski and David L. Darmofal. Review of output-based error estimation and mesh adaptation in computational fluid dynamics. *AIAA Journal*, 49(4):673–694, 2011.
- [19] Markus Geisenhofer, Florian Kummer, and Martin Oberlack. An extended discontinuous Galerkin method for high-order shock-fitting. *arXiv preprint*, 2020.
- [20] Peter Gnoffo. Multi-dimensional inviscid flux reconstruction for simulation of hypersonic heating on tetrahedral grids. In *47th AIAA Aerospace Sciences Meeting including The New Horizons Forum and Aerospace Exposition*, Orlando, Florida, 1/5/2009 – 1/8/2009. American Institute of Aeronautics and Astronautics, AIAA Paper 2009-599.
- [21] Ami Harten, Bjorn Engquist, Stanley Osher, and Sukumar R. Chakravarthy. Uniformly high order accurate essentially non-oscillatory schemes, III. *Journal of Computational Physics*, 131(1):3–47, 1997.
- [22] Ralf Hartmann. Adjoint consistency analysis of discontinuous Galerkin discretizations. *SIAM Journal on Numerical Analysis*, 45(6):2671–2696, 2007.
- [23] Ralf Hartmann and Paul Houston. An optimal order interior penalty discontinuous Galerkin discretization of the compressible Navier–Stokes equations. *Journal of Computational Physics*, 227(22):9670–9685, 2008.
- [24] Ralf Hartmann and Tobias Leicht. Higher order and adaptive DG methods for compressible flows. *37th Advanced CFD Lecture Series: Recent developments in higher order methods and industrial application in aeronautics*, 2014(3):1–156, 2014.
- [25] Tianci Huang, Charles J. Naudet, and Matthew J. Zahr. High-order implicit shock tracking boundary conditions for flows with parametrized shocks. *Journal of Computational Physics*, 495:112517, 2023.
- [26] Tianci Huang and Matthew J. Zahr. A robust, high-order implicit shock tracking method for simulation of complex, high-speed flows. *Journal of Computational Physics*, 454:110981, 2022.
- [27] Guang-Shan Jiang and Chi-Wang Shu. Efficient implementation of weighted ENO schemes. *Journal of Computational Physics*, 126(1):202–228, 1996.
- [28] Eric Johnsen, Johan Larsson, Ankit V. Bhagatwala, William H Cabot, Parviz Moin, Britton J. Olson, Pradeep S. Rawat, Santhosh K. Shankar, Björn Sjögreen, Helen C. Yee, et al. Assessment of high-resolution methods for numerical simulations of compressible turbulence with shock waves. *Journal of Computational Physics*, 229(4):1213–1237, 2010.
- [29] Carl Timothy Kelley and David E. Keyes. Convergence analysis of pseudo-transient continuation. *SIAM Journal on Numerical Analysis*, 35(2):508–523, 1998.
- [30] Andrew D. Kercher and Andrew Corrigan. A least-squares formulation of the moving discontinuous Galerkin finite element method with interface condition enforcement. *Computers & Mathematics with Applications*, 95:143–171, 2021.
- [31] Andrew D. Kercher, Andrew Corrigan, and David A. Kessler. The moving discontinuous Galerkin finite element method with interface condition enforcement for compressible viscous flows. *International Journal for Numerical Methods in Fluids*, 93(5):1490–1519, 2021.
- [32] Theodore Kai Lee and Xiaolin Zhong. Spurious numerical oscillations in simulation of supersonic flows using shock-capturing schemes. *AIAA journal*, 37(3):313–319, 1999.
- [33] Xu-Dong Liu, Stanley Osher, and Tony Chan. Weighted essentially non-oscillatory schemes. *Journal of Computational Physics*, 115(1):200–212, 1994.

- [34] James Lu. *An a posteriori error control framework for adaptive precision optimization using discontinuous Galerkin finite element method*. PhD thesis, Massachusetts Institute of Technology, 2005.
- [35] Katate Masatsuka. *I Do Like CFD*, volume 1. Lulu.com, 2009.
- [36] James M. Modisette. *An automated reliable method for two-dimensional Reynolds-averaged Navier-Stokes simulations*. PhD thesis, Massachusetts Institute of Technology, 2011.
- [37] Gino Moretti. Thirty-six years of shock fitting. *Computers & Fluids*, 31(4-7):719–723, 2002.
- [38] Gino Moretti and Manuel D. Salas. Numerical analysis of viscous one-dimensional flows. *Journal of Computational Physics*, 5(3):487–506, 1970.
- [39] Charles J. Naudet and Matthew J. Zahr. A space-time high-order implicit shock tracking method for shock-dominated unsteady flows. *Journal of Computational Physics*, 501:112792, 2024.
- [40] Jorge Nocedal and Stephen Wright. *Numerical Optimization*. Springer Science & Business Media, 2006.
- [41] Alexander Perez-Reyes and Matthew J. Zahr. An implicit shock tracking method for simulation of shock-dominated flow over complex domains using mesh-based parametrizations. *Journal of Computational Physics*, in review 2025.
- [42] K. Perry and S. Imlay. Blunt-body flow simulations. In *24th Joint Propulsion Conference*, Boston, Massachusetts, 7/11/1988 – 7/13/1988. American Institute of Aeronautics and Astronautics, AIAA Paper 1988-2904.
- [43] Per-Olof Persson and Jaime Peraire. Sub-cell shock capturing for discontinuous Galerkin methods. In *44th AIAA Aerospace Sciences Meeting and Exhibit*, Reno, Nevada, 1/9/2006 – 1/12/2006. American Institute of Aeronautics and Astronautics, AIAA Paper 2006-112.
- [44] J.-Ch. Robinet, Jérémie Gressier, Grégoire Casalis, and J.-M. Moschetta. Shock wave instability and the carbuncle phenomenon: same intrinsic origin? *Journal of Fluid Mechanics*, 417:237–263, 2000.
- [45] Manuel D. Salas. *A Shock-Fitting Primer*. CRC Press, 2009.
- [46] Andrew Shi, P-O Persson, and Matthew J. Zahr. Implicit shock tracking for unsteady flows by the method of lines. *Journal of Computational Physics*, 454:110906, 2022.
- [47] Bram Van Leer. Towards the ultimate conservative difference scheme. V. a second-order sequel to Godunov’s method. *Journal of Computational Physics*, 32(1):101–136, 1979.
- [48] David A. Venditti and David L. Darmofal. Grid adaptation for functional outputs: application to two-dimensional inviscid flows. *Journal of Computational Physics*, 176(1):40–69, 2002.
- [49] David A. Venditti and David L. Darmofal. Anisotropic grid adaptation for functional outputs: application to two-dimensional viscous flows. *Journal of Computational Physics*, 187(1):22–46, 2003.
- [50] Masayuki Yano, James Modisette, and David Darmofal. The importance of mesh adaptation for higher-order discretizations of aerodynamic flows. In *20th AIAA Computational Fluid Dynamics Conference*, pages 2011–3852, 2011.
- [51] Matthew J. Zahr and Per-Olof Persson. An optimization-based approach for high-order accurate discretization of conservation laws with discontinuous solutions. *Journal of Computational Physics*, 365:105 – 134, 2018.
- [52] Matthew J. Zahr and Joseph M. Powers. High-order resolution of multidimensional compressible reactive flow using implicit shock tracking. *AIAA Journal*, 59(1):150–164, December 2020.
- [53] Matthew J. Zahr, Andrew Shi, and P-O Persson. Implicit shock tracking using an optimization-based high-order discontinuous Galerkin method. *Journal of Computational Physics*, 410:109385, 2020.
- [54] Matthew J. Zahr, Andrew Shi, and Per-Olof Persson. Implicit shock tracking using an optimization-based high-order discontinuous Galerkin method. *Journal of Computational Physics*, 410:109385, June 2020.